STATISTICAL PROPERTIES OF CHAOTIC QUANTUM DYNAMICS

By

Kereen Monteyne, H.B.Sc.

A Thesis

Submitted to the School of Graduate Studies

in Partial Fulfillment of the Requirements

for the Degree

Master of Science

McMaster University

MASTER OF SCIENCE (1995) McMaster University

Chemistry

Hamilton, Ontario

TITLE: Statistical Properties of Chaotic Quantum Dynamics

AUTHOR: Kereen Monteyne, H.B.Sc. (McMaster University, Hamilton, Ontario)

SUPERVISOR: Randall S. Dumont

NUMBER OF PAGES: x, 86

ABSTRACT

The statistical properties of T-shaped Ar_3 energy eigenvalues and eigenfunctions are investigated and are used to characterize the system as quantum chaotic. The statistical properties of quantum chaos suggest a statistical theory of quantum dynamics. This statistical quantum dynamics is proposed as an alternative to full scale numerical simulation of quantum dynamics which requires the manipulation of very large matrices. Sparse matrix technology has made the latter computations more tractable; however, a simple alternative based on statistical approximations is still very desirable. The newly proposed statistical theory is tested against sparse-matrix based numerical simulation of the T-shaped Ar_3 inversion dynamics. The unsuccessful results are rationalized in terms of correlations between eigenfunctions not represented in the statistical theory.

ACKNOWLEDGEMENTS

I would like to express my gratitude to my supervisor Dr. Randall S. Dumont for providing me with a research project having many interesting facets. Although at times aspects of the project proved frustrating, the overall experience was very rewarding.

I would most especially like to thank Dr. Anthony Basile for his wisdom, his patience in teaching me the "ways" of quantum mechanics, and for expanding my world beyond these four walls.

Words seem inconsequential when it comes to thanking the friends I've made over the past six years. It's been a long and bumpy road and I feel lucky to have travelled it with some good people.

To Pippa Lock and Jessica Kowanetz:

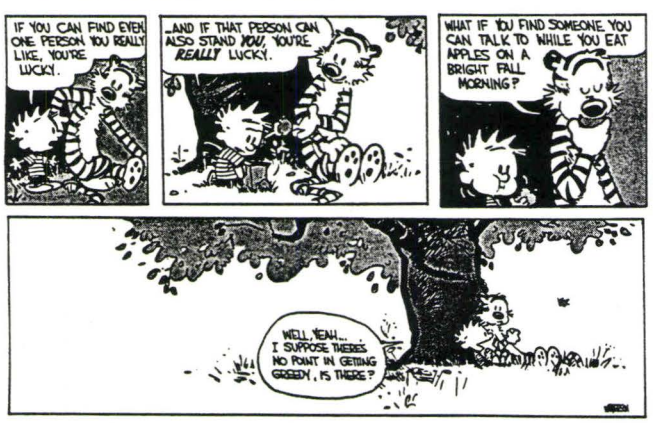

I have found two such people.

Finally, I would like to acknowledge my family back home who to this day still refer to me as the one in university taking "science"; it was necessary to escape there periodically and be a daughter/sister/auntie instead of a student.

TABLE OF CONTENTS

LIST OF TABLES

LIST OF FIGURES

PART I

Introduction

PART I

Introduction

Fully quantum mechanical studies of chemical reactions are usually an idealistic enterprise. The description of the simultaneous and frequently inseparable motions of atoms and molecules by standard quantum mechanical procedures is a formidable challenge which is often simply out of reach. New methodologies like the discrete variable representation have seen the beginnings of an *ab initio* quantum chemistry for simple chemical reactions. However, it is the purpose of this work to develop an alternative approach to quantum molecular dynamics which avoids manipulations of a Hamiltonian matrix. Investigations of quantum systems have found certain characteristic statistical properties of the eigenvalues and eigenfunctions which are indicative of the dynamics for the classical analogue. In principle, these properties permit evaluation of dynamical observables which is more computationally efficient than the standard methods.

The difficulty with quantum dynamics arises from the very large computational scale involved when dealing with large matrices. Even with the accelerating trend of high speed and mass storage computers, the demands of quantum molecular dynamics are still formidable for systems containing more than a few atoms. The last decade has seen substantial progress in the ability to carry out accurate quantum mechanical calculations. Light and co-workers [LHL-85] have lead the way with discrete variable representation methods which offer many advantages over traditional methods. The discrete variable representation finds easy to construct Hamiltonian

matrices which are very sparse. This latter property considerably simplifies the resulting linear algebra calculations for the eigenvalues and eigenfunctions. Nevertheless, a full dimensional quantum mechanical treatment of molecular dynamics is still a time and memory expensive venture. A new "quantum statistical mechanics" is proposed as a means of extracting dynamical observables. This approach has its origins in the behaviour of the dynamics for the classical counterpart to a quantum system.

The terms "regular" and "chaotic" are used to describe two qualitatively distinct types of dynamics. In classical mechanics, the criteria for classifying the dynamics are well understood, but the same cannot be said for quantum mechanics. The characterization of quantum dynamics has mainly been statistical in nature; focusing on the properties of the energy eigenvalues and eigenfunctions. The results of various studies suggest universal characteristics in the statistical properties of the energy eigenvalues and eigenfunctions which can be related to the associated classical dynamics. Specifically, the energy level fluctuations in a quantum spectrum are described by a Poisson or Wigner distribution for regular or chaotic motion, respectively, of the classical analogue. The eigenfunctions corresponding to a classically chaotic system were conjectured by Berry [Be-77] to be independent Gaussian random functions of position with a spatial pair-correlation function expressable as a Bessel function. The quantum study of a classically chaotic system is commonly referred to as quantum chaos. Research in this area has been primarily devoted to the understanding of the quantum manifestations of classical chaos. The next logical step would be to ask the question: if a quantum system exhibits the characteristic statistical properties corresponding to classically chaotic dynamics, can this knowledge be used to advantage?

A study of the inversion process exhibited by the T-shaped trimer, Ar_3, is pre-

sented here as its corresponding classical dynamics is strongly chaotic [BLB-88]. Part II begins with a description of the T-shaped Ar_3 quantum system. The Hamiltonian is constructed in the discrete variable representation with the symmetry properties of the molecule exploited so as to reduce the computational scale of the matrix diagonalization for the eigenvalues and eigenfunctions. The predicted statistical properties are assessed in Part III by computing the successive level spacing distribution of the energy spectrum along with the spatial distribution and the spatial pair-correlation function of the energy eigenfunctions. In Part IV, the inversion process is characterized by its survival probability. The inherent chaos of the quantum dynamics is used as a tool to develop a statistical model to the survival probability. Although the statistical model falls short of reproducing the observed quantum survival probability, the insight gained into the statistical theory should guide future work towards a more viable method.

PART II

T-Shaped Ar_3

PART II

T-Shaped Ar_3

The trimer of argon, a closed shell atom, is held together only by Van der Waals' interactions. As a result, Ar_3 is not amenable to treatment by separable or adiabatic approximations. The trimer is restricted to a T-shaped geometry which determines a two degree of freedom Hamiltonian system.

II.1 The Hamiltonian

In terms of mass-scaled coordinates (x, y), the two degree of freedom Hamiltonian is given by

$$\hat{H}(x,y) = \frac{\hat{p}_x^2}{2} + \frac{\hat{p}_y^2}{2} + \hat{V}(x,y) \quad . \tag{1}$$

This Hamiltonian permits a simple intramolecular inversion process wherein the equatorial argon atom passes between the other two atoms, as depicted in Figure 1. From the diatomic Ar_2 potential of Aziz and Slaman [AS-86], a three body potential is constructed using only two body interactions. The inversion threshold, E_{thres}, is given by the Ar_3 saddle point energy of $140.38K$ [1], and the dissociation energy, E_{diss}, is $286.448K$ [1].

II.1.1 The Discrete Variable Representation

A discrete variable representation (DVR) is used to construct the Hamiltonian matrix. The DVR [LHL-85] is a grid-point representation with the following advantages; the Hamiltonian matrix elements are trivially evaluated with none of the usual integral evaluations, and more importantly, a DVR produces sparse matrices.

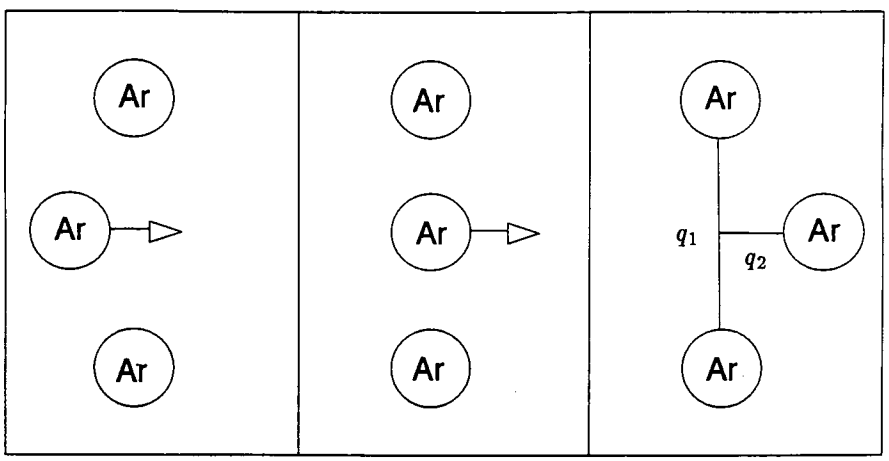

FIGURE 1. The inversion process of T-shaped Ar_3 wherein one of the argon atoms is constrained to move along the perpendicular bisector of the bond associated with the other two atoms. This constrained system has two degrees of freedom, q_1 and q_2. Mass-scaled coordinates are constructed via $x = q_2\sqrt{m_{q_2}}$, $y = q_1\sqrt{m_{q_1}}$, with the reduced masses $m_{q_2} = 2m_{Ar}/3$ and $m_{q_1} = m_{Ar}/2$.

The latter characteristic greatly simplifies Hamiltonian matrix diagonalization. The elements of the kinetic and potential matrices result from a comparison of two points, $i = (x_i, y_i)$ and $j = (x_j, y_j)$, taken from a specified grid in configuration space.

In all DVR methods the potential energy matrix is taken to be diagonal,

$$V_{i,j} = V_{(x_i,y_i),(x_j,y_j)}\ \delta_{i,j} \tag{2}$$

$$V_{i,j} = \begin{pmatrix} V(x_1,y_1) & 0 & \cdots & 0 \\ 0 & V(x_2,y_2) & \ddots & \vdots \\ \vdots & \ddots & \ddots & 0 \\ 0 & \cdots & 0 & V(x_n,y_n) \end{pmatrix} \quad ,$$

where $\{\,(x_j, y_j)\,\}_{j=1}^{n}$ is the set of configuration space grid-points. For a uniformly spaced grid the associated basis functions are the Fourier functions [CM-92]

$$< x, y|i > = < x|x_i > < y|y_i > = \frac{\sin(\frac{\pi[x-x_i]}{\Delta x})}{\pi[x-x_i]} \frac{\sin(\frac{\pi[y-y_i]}{\Delta y})}{\pi[y-y_i]} \quad , \tag{3}$$

where $\Delta x, \Delta y$ are the grid spacings in the respective directions. Note that these functions are L^1-normalized. The potential energy matrix element in terms of the L^2-normalized basis $< x|x_i >_2 = \sqrt{\Delta x} < x|x_i >$ is given by

$$V_{i,j} = \int_{-\infty}^{\infty} dx\ dy\ \langle x|x_i\rangle_2 \langle y|y_i\rangle_2 \hat{V}(x,y)\ \langle x|x_j\rangle_2 \langle y|y_j\rangle_2 \quad , \tag{4}$$

and is truly diagonal only in the limit of an infinite grid as

$$\lim_{\Delta x \to 0} \langle x|x_i\rangle = \delta(x - x_i) \quad . \tag{5}$$

If the potential varies slowly over the range of integration, then the simple multiplication operator $\hat{V}(x,y) = V(x,y)$ can be taken outside the integral in equation (4) to give a diagonal matrix in the orthogonal basis, as integration of $\langle x|x_i\rangle\ \langle x|x_j\rangle = 0$ for $i \neq j$.

The primary novel feature of a DVR is that it gives an extremely simple kinetic energy matrix. The kinetic energy operator contains second order differentials which are approximated by an infinite order finite difference equation. In one

dimension the kinetic energy operator is given by

$$T_{i,j} = \frac{\hbar^2(-1)^{i-j}}{2(\Delta x)^2} \begin{cases} \pi^2/3 & i = j \\ 2/(i-j)^2 & i \neq j \end{cases} , \tag{6}$$

where the only parameter involved is the grid spacing, Δx. The key to the simplicity of the kinetic energy operator in the discrete variable representation is that it is diagonal in all but one direction; specifically,

$$\hat{T}_x = T_{x_i,x_j}\, \delta_{y_i,y_j} \tag{7}$$

$$\hat{T}_x = \begin{pmatrix} T_{(x_1,x_1)} & \cdots & T_{(x_1,x_n)} & 0 & \cdots & 0 & 0 & \cdots & 0 \\ \vdots & \ddots & \vdots & \vdots & \ddots & \vdots & \vdots & \ddots & \vdots \\ T_{(x_n,x_1)} & \cdots & T_{(x_n,x_n)} & 0 & \cdots & 0 & 0 & \cdots & 0 \\ 0 & \cdots & 0 & \ddots & & & 0 & \cdots & 0 \\ \vdots & \ddots & \vdots & & \ddots & & \vdots & \ddots & \vdots \\ 0 & \cdots & 0 & & & \ddots & 0 & \cdots & 0 \\ 0 & \cdots & 0 & 0 & \cdots & 0 & T_{(x_1,x_1)} & \cdots & T_{(x_1,x_n)} \\ \vdots & \ddots & \vdots & \vdots & \ddots & \vdots & \vdots & \ddots & \vdots \\ 0 & \cdots & 0 & 0 & \cdots & 0 & T_{(x_n,x_1)} & \cdots & T_{(x_n,x_n)} \end{pmatrix} ,$$

$$\hat{T}_y = T_{y_i,y_j}\, \delta_{x_i,x_j} \tag{8}$$

$$\hat{T}_y = \begin{pmatrix} T_{(y_1,y_1)} & 0 & \cdots & 0 & & & T_{(y_1,y_n)} & 0 & \cdots & 0 \\ 0 & \ddots & \ddots & \vdots & \cdots & \cdots & 0 & \ddots & \ddots & \vdots \\ \vdots & \ddots & \ddots & 0 & & & \vdots & \ddots & \ddots & 0 \\ 0 & \cdots & 0 & T_{(y_1,y_1)} & & & 0 & \cdots & 0 & T_{(y_1,y_n)} \\ & \vdots & & & \ddots & & & & \vdots & \\ & \vdots & & & & \ddots & & & \vdots & \\ T_{(y_n,y_1)} & 0 & \cdots & 0 & & & T_{(y_n,y_n)} & 0 & \cdots & 0 \\ 0 & \ddots & \ddots & \vdots & \cdots & \cdots & 0 & \ddots & \ddots & \vdots \\ \vdots & \ddots & \ddots & 0 & & & \vdots & \ddots & \ddots & 0 \\ 0 & \cdots & 0 & T_{(y_n,y_1)} & & & 0 & \cdots & 0 & T_{(y_n,y_n)} \end{pmatrix} .$$

The total kinetic energy is clearly a simple and sparse matrix.

One potential concern about the use of an infinite order expression for the kinetic energy operator is that it corresponds to an infinite grid. The decay of the off-diagonal matrix elements is relatively slow, it goes like $(i-j)^{-2}$, as seen in equation (6). Since real calculations must be done on a finite grid, the convention of deleting grid-points where the wavefunction is negligibly small (in energetically inaccessible regions) is adopted. This corresponds to placing the wavefunction in a box whose size and shape is dictated by the grid-points retained and forcing the wavefunction to vanish at all other points. The restriction of the grid size is accomplished by introducing an energy cutoff E_{max} where only grid-points for which $V(x_i, y_i) \leq E_{max}$ are retained. This procedure generates a grid which is automatically adapted to the shape of the potential energy surface. Wavefunctions for states with energies sufficiently below E_{max} will be negligibly small at the discarded grid-points; however, the higher energy states will have the tail of the wavefunction prematurely curtailed. This error in the wavefunction is minimized by enlarging the grid beyond the E_{max} potential energy contour. For a grid-point found with $V(x_i, y_i) > E_{max}$, the minimum imaginary action W_i is calculated along the steepest descent path to the contour defined by E_{max}. The grid-points for which $W_i > W_{max}$ are retained where W_{max} is chosen such that $\exp\left(\frac{-W_{max}}{\hbar}\right)$, which resembles a wavefunction value, is a sufficiently small number. In this manner, additional grid-points are included beyond the E_{max} potential energy contour with the majority occurring in regions where the potential does not change rapidly, as seen in Figure (2).

II.1.2 Symmetry

The potential energy is symmetric about $x = 0$; $V(x, y) = V(-x, y)$. This symmetry can be exploited to reduce the computational scale of the Hamiltonian matrix diagonalization. Since the Hamiltonian operator $\hat{H}$ has the same symmetry as

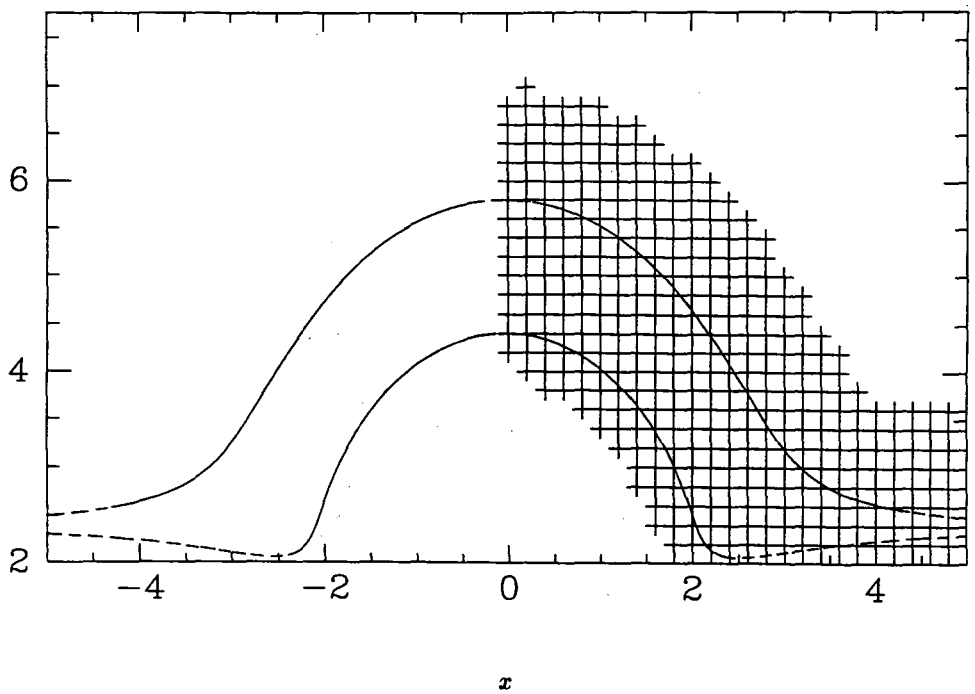

FIGURE 2. Potential energy contour for $V(x_i, y_i) = E_{max} = 286K$. The grid-points beyond this contour are retained if the value of the imaginary action W_i along the steepest descent path to the E_{max} contour is less than W_{max}. The majority of the additional grid-points occur in the regions where the potential does not vary rapidly, *i.e.*, regions where x and y are large.

the potential energy operator (the kinetic energy operator is symmetric with respect to any translation or reflection) then the wavefunctions, ψ, must be eigenfunctions of the reflection through $x = 0$ operator, $\hat{R}$

$$\hat{R}\psi = r\psi \qquad ; \text{ eigenvalues } r = \pm 1 \quad . \tag{9}$$

Thus, the unique values of the wavefunction $\psi(x, y)$ are contained on $x \geq 0$ (or $x \leq 0$) as its reflection $\psi(-x, y)$ is either the same or opposite in sign. All information about the wavefunction can be obtained by constructing the Hamiltonian in a DVR having only grid-points with $x_i \geq 0$. The computational scale has now been effectively reduced to almost half the number of grid-points.

The symmetry in the Hamiltonian determines two types of real wavefunctions; a symmetric ,ψ^s, and an anti-symmetric ,ψ^a. The symmetric wavefunction determines an eigenvalue $r = 1$ for the reflection operator, while the anti-symmetric wavefunction determines the eigenvalue of $r = -1$. At energies $E < E_{thres}$ the height of the isomerization potential barrier almost separates the system into two potential well problems, each determining its own set of eigenvalues and eigenfunctions. Since these two potential wells are symmetric, the two sets of eigenvalues occur at almost the same energies resulting in nearly degenerate pairs of eigenvalues at below threshold energies for the total system. To explain the degeneracy in the below threshold paired energy levels and its disappearance at higher energies, consider the energy difference between the symmetric and anti-symmetric eigenvalues,

$$\Delta E_j = E_{j_s} - E_{j_a} \quad . \tag{10}$$

Both the symmetric and anti-symmetric energies can be expressed in the form

$$E_j = \int dx\, dy\, \psi^j \hat{H}\, \psi^j \quad . \tag{11}$$

Because of the symmetry in the potential energy, the j^{th} symmetric and anti-symmetric eigenfunctions are almost identical except in the small interval Ω about $x = 0$. Thus, the only contributions to ΔE will occur in this interval. Potential energy contributions to E_{j_s} and E_{j_a} cancel because

$$|\psi^{j_s}|^2 \simeq |\psi^{j_a}|^2 \quad ; \tag{12}$$

therefore, only the kinetic energy gives rise to the energy differences. In particular, only the $\frac{\partial^2}{\partial x^2}$ type contribution need be considered since ψ^{j_s} and ψ^{j_a} have similar relative curvatures in the y direction. Because ψ^{j_a} changes sign upon going through $x = 0$, it is approximated as linear in the Ω interval, thus

$$\psi^{j_a} \hat{H} \psi^{j_a} \rightarrow \psi^{j_a} \hat{T} \psi^{j_a} \rightarrow -\psi^{j_a} \frac{\partial^2}{\partial x^2} \psi^{j_a} = 0 \quad . \tag{13}$$

As ψ^{j_s} has relative postive curvature in the Ω interval, then

$$\psi^{j_s} \hat{H} \psi^{j_s} \rightarrow \psi^{j_s} \hat{T} \psi^{j_s} \rightarrow -\psi^{j_s} \frac{\partial^2}{\partial x^2} \psi^{j_s} < 0 \quad , \tag{14}$$

and the energy difference ΔE is

$$\Delta E_j = E_{j_s} - E_{j_a} < 0 \quad . \tag{15}$$

The splitting between the j^{th} symmetric and anti-symmetric levels increases as the energy increases because of the increasing relative positive curvature in ψ^{j_s} in the Ω interval about $x = 0$.

Constructing the Hamiltonian in a DVR using grid-points with $x_i \geq 0$ to determine both the symmetric and anti-symmetric levels could lead to mixing in these states when they are close in energy. This mixing problem is avoided by using a new "symmetrized" DVR basis $< x, y|i' >$ defined in terms of the usual DVR basis functions $< x, y|i >$ as

$$< x, y|i' > = K \left\{ < x, y|i > \pm < x, y|\hat{R}i > \right\} \quad , \tag{16}$$

where $\hat{R}i$ is the point $i = (x_i, y_i)$ reflected through $x = 0$, K is a normalization constant, and $< x, y|i >$ is defined as in equation (3). This symmetrized basis requires that the Hamiltonian is constructed only on grid-points having $x_i \geq 0$ such that the dimensionality of the Hamiltonian is equal in the two basis sets. The advantage of the symmetrized basis is that it block diagonalizes the Hamiltonian into a symmetric Hamiltonian $\hat{H}_s$, which gives the symmetric eigenvalues and eigenfunction co-efficients at each of the grid-points and an anti-symmetric Hamiltonian $\hat{H}_a$, which gives the anti-symmetric eigenvalues and eigenfunction co-efficients. These two blocks can be diagonalized separately, effectively eliminating the mixing problem. Since the Hamiltonians are very sparse, Lanczos-type or iterative linear algebra methods are ideally suited to the eigenvalue analysis.

II.1.3 Normalization

Let q be the co-ordinates of a quantum system. The state of the system is described by the wavefunction, $\Phi^i(q)$. The probability that a measurement performed on the system will find the values of the co-ordinates in the element dq of configuration space is $|\Phi^i(q)|^2\, dq$. The sum of these probabilities must be equal to unity

$$\int_{-\infty}^{\infty} dq\, \Phi^{i*}(q)\, \Phi^j(q) = \delta_{i,j} \quad ; \tag{17}$$

this is called the normalization condition. In the case of a discrete spectrum an arbitrary state Φ^i can be represented by the series

$$\Phi^i(q) = \sum_n a_n^i\, \phi_n(q) \quad , \tag{18}$$

where a_n are constants and the $\phi_n(q)$ are basis functions. The normalization condition is now given by

$$\sum_n (a_n^i)^*\, a_n^j = \delta_{i,j} \quad , \tag{19}$$

if the $\phi_n(q)$ are orthonormal, *i.e.*,

$$\int_{-\infty}^{\infty} dq\ \phi_n^*(q)\ \phi_m(q) = \delta_{n,m} \quad . \tag{20}$$

Now, the symmetrized DVR basis function $< x, y|i' >$, while orthogonal but not orthonormal, is defined such that the value of the wavefunction at a grid-point is given in terms of the co-efficient at that grid-point. Namely, the expansion over the DVR grid-points $i = (x_i, y_i)$ having $x_i \geq 0$ in terms of the symmetrized DVR basis functions is

$$\psi^j(x,y) = \sum_{i,(x_i \geq 0)} c_i^j < x, y|i' > \quad , \tag{21}$$

where

$$< x, y|i' > = \begin{cases} \frac{1}{\sqrt{2}} \left\{ < x, y|i > \pm < x, y|\hat{R}i > \right\} & x_i \neq 0 \\ < x, y|i > & x_i = 0 \end{cases} \quad , \tag{22}$$

with $< x, y|i >$ defined in equation (3); at a grid-point (x_l, y_l),

$$\psi^j(x_l, y_l) = \sum_{i,(x_i>0)} c_i^j \frac{1}{\sqrt{2}} \left\{ < x_l, y_l|i > \pm < x_l, y_l|\hat{R}i > \right\} + \sum_{i,(x_i=0)} c_i^j < x_l, y_l|i > \quad . \tag{23}$$

Since $\frac{x_l - x_i}{\Delta x} \in \aleph$, then

$$\frac{\sin\left[\frac{\pi(x_l - x_i)}{\Delta x}\right]}{\pi(x_l - x_i)} = \frac{\delta_{x_l, x_i}}{\Delta x} \quad , \tag{24}$$

and the expansion of the DVR basis functions $< x_l, y_l|i >$ in equation (23) becomes

$$\psi^j(x_l, y_l) = \sum_{i,(x_i>0)} \frac{c_i^j}{\sqrt{2}} \left\{ \frac{\delta_{x_l,x_i}}{\Delta x} \frac{\delta_{y_l,y_i}}{\Delta y} \pm \frac{\delta_{x_l,\hat{R}x_i}}{\Delta x} \frac{\delta_{y_l,\hat{R}y_i}}{\Delta y} \right\} + \sum_{i,(x_i=0)} c_i^j \frac{\delta_{x_l,x_i}}{\Delta x} \frac{\delta_{y_l,y_i}}{\Delta y} \quad ; \tag{25}$$

the condition $x_l = \hat{R}x_i$ is never satisfied, therefore the second term of the $x_i > 0$ sum in equation (25) is zero. The value of the wavefunction at a grid-point is now given by

$$\psi^j(x_l, y_l) = \begin{cases} \frac{c_l^j}{\sqrt{2}\Delta x \Delta y} & x_l > 0 \\ \frac{c_l^j}{\Delta x \Delta y} & x_l = 0 \end{cases} \quad , \tag{26}$$

where c_l^j is the co-efficient to the j^{th} eigenfunction at the grid-point $l = (x_l, y_l)$. The normalization condition for $\psi^j(x,y)$ expanded in the symmetrized DVR basis becomes

$$\int_{-\infty}^{\infty} dx\ dy\ \psi^{j\,*}(x,y)\ \psi^k(x,y) = \sum_{i,(x_i \geq 0)} \frac{c_i^j c_i^k}{\Delta x \Delta y} = \delta_{j,k} \quad ; \tag{27}$$

the details of the integration are presented in Appendix A. The co-efficients $\{c_i^j\}_{i=1}^n$ resulting from the matrix diagonalization must then be scaled such that

$$\sum_{i,(x_i \geq 0)} (c_i^j)^2 = \Delta x \Delta y \quad , \tag{28}$$

so that the wavefunction $\psi^j(x,y)$ expanded in terms of the symmetrized DVR basis satisfies the normalization condition.

II.2 Energy Eigenvalues and Eigenfunctions

The energies and wavefunctions for the bound states of T-shaped Ar_3 are computed for energies up to $286K$, where dissociation of the trimer occurs at $286.448K$. The Hamiltonian is evaluated in the discrete variable representation with the symmetry of the potential energy utilized in order to reduce the computational burden of the two degree of freedom problem.

As a function of the grid spacing Δx, the convergence study of the energy levels is shown in Table 1.

	Δx (ms-Bohr)			
$j_s\,(E'_{j_s}(K))$	0.25(0.034)	0.20(0.027)	0.15(0.016)	0.10(0.013)
1 $(44.96K)$	7.6×10^{-2}	-2.9×10^{-2}	-2.2×10^{-4}	-3.0×10^{-7}
8 $(142.64K)$	1.2×10^{-2}	1.1×10^{-2}	-7.5×10^{-4}	2.1×10^{-6}
15 $(165.02K)$	3.3×10^{-2}	-5.9×10^{-3}	-2.9×10^{-3}	2.9×10^{-6}
25 $(191.53K)$	1.3×10^{-2}	4.4×10^{-3}	-2.8×10^{-3}	7.3×10^{-7}
50 $(237.46K)$	6.6×10^{-2}	3.8×10^{-3}	-1.4×10^{-3}	-2.9×10^{-5}
65 $(259.63K)$	9.7×10^{-2}	1.7×10^{-2}	2.0×10^{-3}	-4.2×10^{-4}

TABLE 1. Relative error $\frac{E_{j_s} - E'_{j_s}}{E'_{j_s}}$ of the symmetric energy levels as a function of the grid spacing in the x-direction. The "exact" eigenvalue E'_{j_s} is taken from the $\Delta x = 0.05$ DVR grid. The corresponding anti-symmetric eigenvalues show the same convergence properties. The grid spacings are in mass-scaled units [1], but the corresponding value in standard units (nm) is shown in parentheses. For comparison, the equilibrium configuration in the potential well occurs at $x = 2.8$ ms-Bohr or 0.38 nm.

Table 1 shows that a smaller grid spacing is required to achieve a given level of accuracy for the higher quantum states. This result is not unexpected because the higher states have a shorter minimum de Broglie wavelength. De Broglie's hypothesis states that an object traveling with velocity v ($v = p$ in mass-scaled units) is associated with the wavelength

$$\lambda_{min} = \frac{h}{p} \quad . \tag{29}$$

The minimum de Broglie wavelength corresponds to a maximum kinetic energy,

$$T = \frac{p_x^2}{2} + \frac{p_y^2}{2} \quad . \tag{30}$$

If the kinetic energy is concentrated mainly in one direction, say the x-direction, then the wavelength of the wavefunction in the region of the bottom of the potential well where $V \simeq 0$ is

$$\lambda_{min} = \frac{h}{p_x} \rightarrow E = \frac{p_x^2}{2} \rightarrow \lambda_{min} = \frac{h}{\sqrt{2E}} \quad . \tag{31}$$

The accuracy in the quantum state can be expressed in terms of the number of grid-points per minimum de Broglie wavelength,

$$\eta = \frac{\lambda_{min}}{\Delta x} \quad . \tag{32}$$

Substituting the expression for λ_{min} from equation (31), then

$$\eta = \frac{h}{\sqrt{2E}\Delta x} \quad . \tag{33}$$

Table 2 shows the relative error of the energy levels as a function of the number of grid-points per minimum de Broglie wavelength. To achieve a relative accuracy of 10^{-3} to 10^{-4}, then the rapidly oscillating part of the quantum state should be represented by 2 to 3 grid-points. The estimate of the number of grid-points in the x-direction is actually too low because there is energy partitioned into the y-direction, resulting in a lower energy term in equation (33). This method of choosing

an appropriate grid spacing for the energy range of interest turns out not to be the most efficient. While it represents the rapidly oscillating part of the wavefunction with sufficient grid-points to determine a desired level of accuracy in the high energy states, there is oversampling (too many grid-points) of the wavefunction in regions where it does not vary as rapidly.

	Δx (ms-Bohr)			
j_s	0.25(0.034)	0.20(0.027)	0.15(0.016)	0.10(0.013)
1	10^{-2} : 2.6	10^{-2} : 3.3	10^{-4} : 4.4	10^{-7} : 6.6
8	10^{-2} : 1.5	10^{-2} : 1.9	10^{-4} : 2.5	10^{-6} : 3.7
15	10^{-2} : 1.4	10^{-3} : 1.7	10^{-3} : 2.3	10^{-6} : 3.5
25	10^{-2} : 1.3	10^{-3} : 1.6	10^{-3} : 2.1	10^{-7} : 3.2
50	10^{-2} : 1.2	10^{-3} : 1.4	10^{-3} : 1.9	10^{-5} : 2.9
65	10^{-2} : 1.1	10^{-2} : 1.4	10^{-3} : 1.8	10^{-4} : 2.8

TABLE 2. Relative error of the symmetric energy levels as a function of the number of grid-points per minimum de Broglie wavelength in the x-direction (relative error : η). The grid spacings are in mass-scaled units [1], but the corresponding value in standard units (nm) is shown in parentheses.

In effect, a uniform grid with a grid spacing chosen by the above method produces a more computationally intensive problem than by using a non-uniform grid where the grid spacing is determined by the rate of oscillation in the high energy states. A non-uniform grid growing procedure is now under consideration, and its benefits will be realized in similar calculations on heavier atoms and especially in semi-classical limit calculations ($\hbar \to 0$). In the latter case, the grid spacing must be reduced by the same factor as $\hbar$ in order to achieve the same level of accuracy.

Figures (3) and (4) show contour plots of selected wavefunctions for the T-shaped Ar_3 system. Figure (3) clearly illustrates the near degeneracy of the below threshold eigenstates.

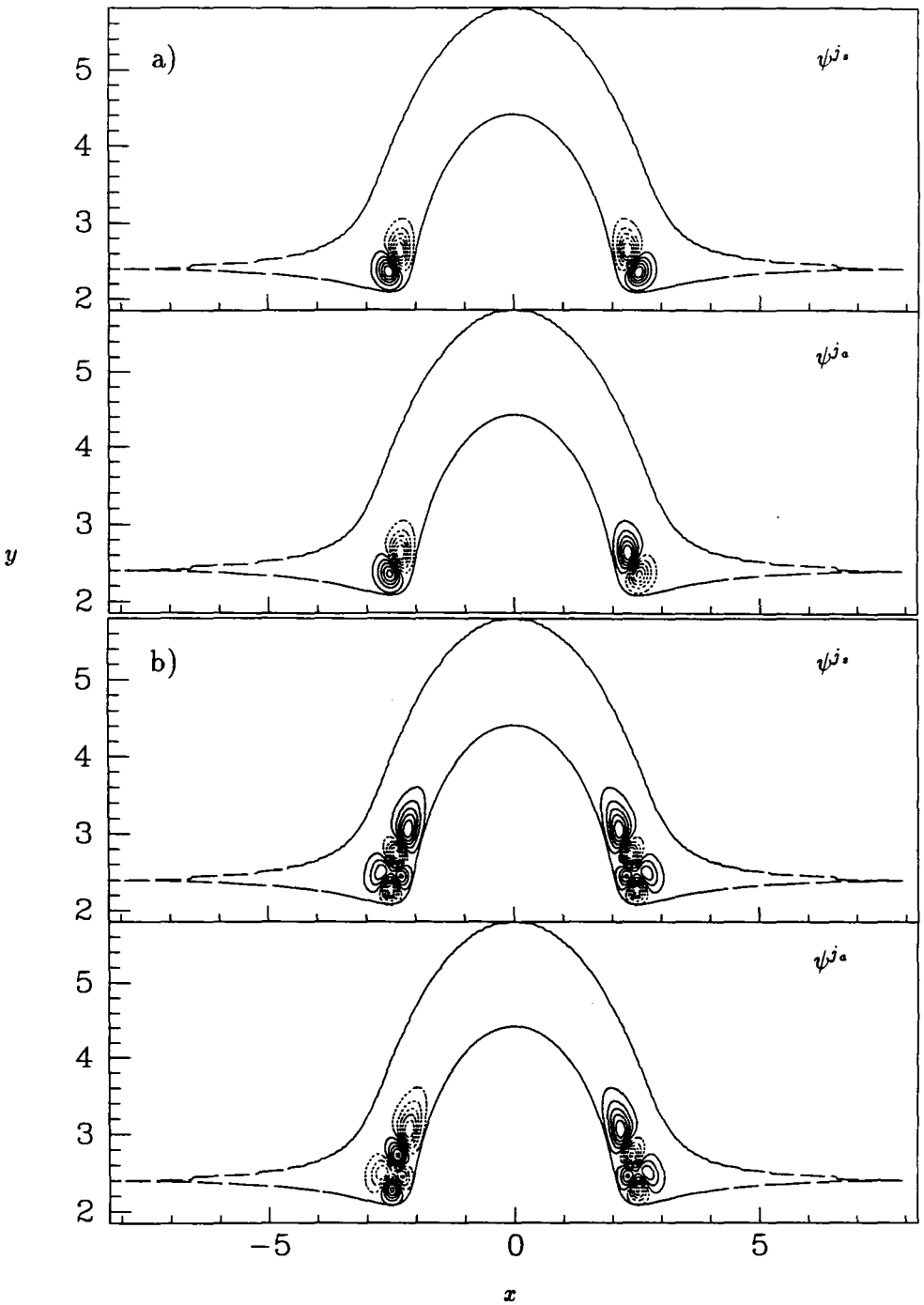

FIGURE 3. Wavefunction contours for the symmetric eigenstate ψ^{j_s} with the corresponding closest in energy paired anti-symmetric eigenstate ψ^{j_a} : a) $j_s = 2$ $(E_{j_s} = 77.74K)$, b) $j_s = 6$ $(E_{j_s} = 129.08K)$. The solid contours correspond to a positive phase in the wavefunction, and the dotted contours correspond to a negative phase in the wavefunction.

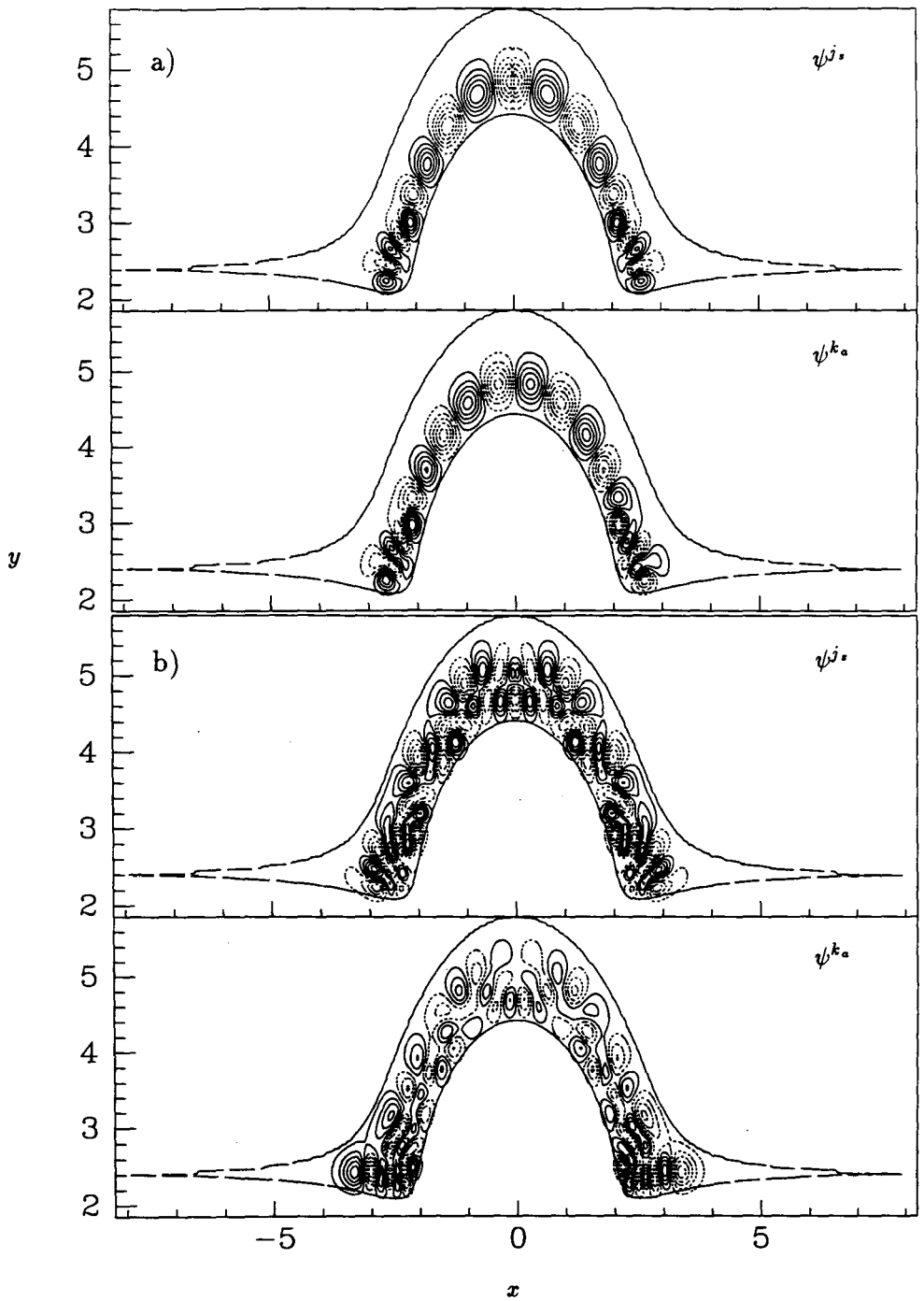

FIGURE 4. Wavefunction contours for the symmetric eigenstate ψ^{j_s} with the corresponding closest in energy anti-symmetric eigenstate ψ^{k_a} : a) $j_s = 15$ $(E_{j_s} = 165.02K)$, b) $j_s = 50$ $(E_{j_s} = 237.46K)$. The solid contours correspond to a positive phase in the wavefunction, and the dotted contours correspond to a negative phase in the wavefunction.

PART III

Quantum Chaos of T-Shaped Ar_3

PART III

Quantum Chaos of T-Shaped Ar_3

The search for quantum manifestations of classical chaos has attracted much interest in recent years. While the criteria for classical chaos are well established, much less is known about quantum chaos. Investigations into quantum chaos typically focus on statistical properties of energy eigenvalues and eigenfunctions [Be-77, BG-84]. Numerical evidence indicates certain universal characteristics of these statistics in the case of quantum analogues to classically chaotic systems [LSW-92, DG-86, BGS-84].

III.1 Energy Eigenvalue Statistical Properties

Is classical chaos manifest in the energy eigenvalue spectrum? It has long been observed that the energy eigenvalue spectra of quantum analogues to classically chaotic systems are qualitatively different from the "regular spectra" which correspond to regular classical dynamics. Specifically, the "chaotic spectra" exhibit level repulsion – small successive level spacings are very rare, in contrast to the frequent near degeneracies seen in the regular spectra. Berry and Tabor [BT-77] showed that the successive level spacing distribution for a regular spectrum is described by a universal Poisson distribution

$$P_p(s) = \frac{\exp\left(\frac{-s}{D}\right)}{D} \quad , \tag{34}$$

in the semi-classical limit. Here, s is a spacing in an appropriately scaled form of the spectrum and D is the associated mean level spacing. The scaled spectrum is

constructed so as to remove the bias introduced by systematic variations in the level density. The resulting mean level density is uniformly unity. In this case, the Poisson distribution is simply $\exp(-s)$.

Quantum chaos has been identified with another quite different scaled level spacing distribution. In particular, systems which have strongly chaotic classical analogues typically have a Wigner successive level spacing distribution [Wi-56],

$$P_W(s) = \frac{\pi s}{2} \exp\left(\frac{-\pi s^2}{4}\right) \quad . \tag{35}$$

This is the distribution expected for eigenvalues of a Gaussian orthogonal ensemble of random matrices.

The details of the energy level scaling needed to reveal the universal spacing distributions are examined in the following section. Specifically, the scaled spectrum is given by $\overline{N(E_j)}$ where $\overline{N(E)}$ is the "average" cumulative density of states.

III.1.1 Cumulative Density of States

The average cumulative density, or number of energy levels below the energy E is expressed as

$$\overline{N(E)} = \int_0^E dE' \, \overline{\rho(E')} \quad , \tag{36}$$

where

$$\overline{\rho(E)} = \frac{1}{h^2} \int_{-\infty}^{\infty} dp_x \, dp_y \int_{-\infty}^{\infty} dx \, dy \; \delta(E - H) \quad , \tag{37}$$

is Weyl's semi-classical formula for the average density of eigenstates per unit interval of energy; H is the classical Hamiltonian. The notation $\overline{\prime\prime}$ denotes an ensemble average value. Substitution of the classical analogue to the T-shaped Ar_3 system Hamiltonian from equation (1) permits direct integration over p_x and p_y, resulting in

$$\overline{\rho(E)} = \frac{2\pi}{h^2} \int_{-\infty}^{\infty} dx \, dy \; \Theta(E - V(x,y)) \quad , \tag{38}$$

where $\Theta(E - V(x,y))$ is a Heaviside function defined by

$$\Theta(E - V(x,y)) = \begin{cases} 1 & E > V(x,y) \\ 0 & E < V(x,y) \end{cases} \quad . \tag{39}$$

Substitution of equation (38) into equation (36) and discretizing the integral to the DVR grid determines the average number of energy levels below the energy E for the T-shaped Ar_3 system;

$$\overline{N(E)} = \frac{2\pi}{h^2} \Delta x \, \Delta y \left\{ \sum_{i,(x_i>0)} 2\,[E - V(x_i,y_i)]_+ + \sum_{i,(x_i=0)} \frac{1}{2}\,[E - V(x_i,y_i)]_+ \right\} \quad , \tag{40}$$

where the notation ["]$_+$ means that only grid-points for which $E - V(x_i,y_i) \geq 0$ contribute to the sums.

The actual quantum density of eigenstates consists of a series of δ-functions

$$\rho(E) = Tr\,[\delta(E - \hat{H})] = \sum_j \delta(E - E_j) \quad , \tag{41}$$

leading to the cumulative density of eigenstates given by

$$N(E) = \int_0^E dE'\, \rho(E') = \sum_j \Theta(E - E_j) \quad . \tag{42}$$

Figure (5) shows the stair-case like function $N(E)$ and the continuous function $\overline{N(E)}$ for the T-shaped Ar_3 system. The exact function $N(E)$ is fitted very closely by the smoothing approximation $\overline{N(E)}$. The disagreement at high energies can be attributed to the incomplete convergence of the high energy states.

The symmetry in the T-shaped Ar_3 Hamiltonian divides the spectrum into two parts; the symmetric and the anti-symmetric energy levels. As already seen, these different symmetries arise from different boundary conditions associated with energy eigenfunctions defined on the desymmetrized space, $x \geq 0$. The average cumulative densities $\overline{N_s(E_{j_s})}$ and $\overline{N_a(E_{j_a})}$ are evaluated for each spectrum separately in terms of appropriate semi-classical approximations to the quantum density of states, $\rho(E)$.

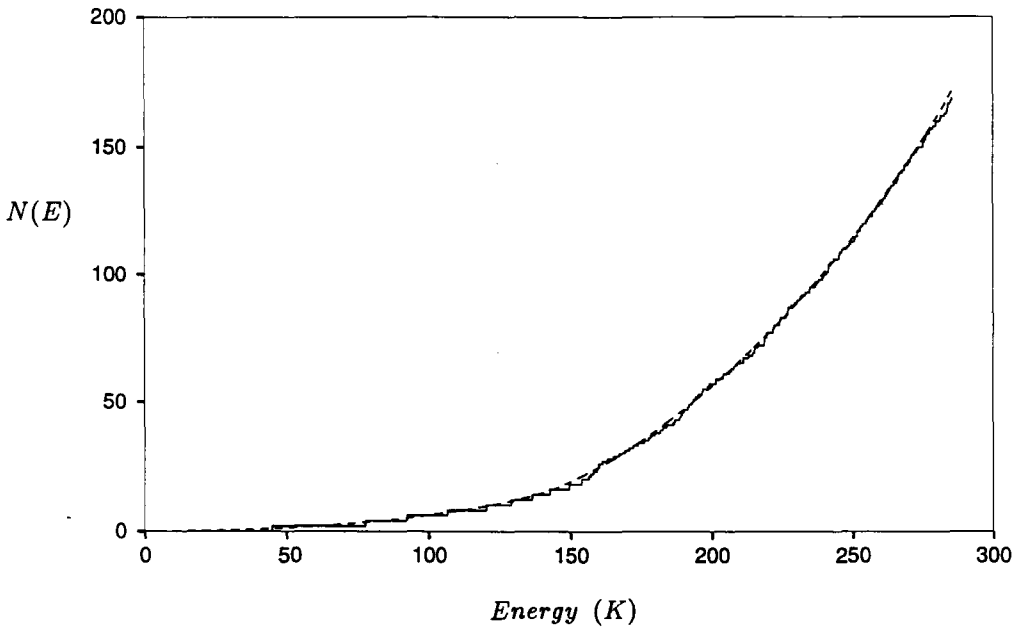

FIGURE 5. The cumulative density of states $N(E)$ (solid) and its semi-classical approximation $\overline{N(E)}$ (dashed) for the T-shaped Ar_3 energy spectrum.

The quantum mechanical trace of equation (41) is performed on the unique values of $\psi(x_i, y_i)$ which occur on grid-points having $x_i \geq 0$ (or $x_i \leq 0$). Inserting the Fourier representation of the δ-function, the quantum density of states becomes

$$\rho(E) = Tr\left[\frac{1}{\hbar}\int_{-\infty}^{\infty} dt\, \exp\left(\frac{i(E-\hat{H})t}{\hbar}\right)\right] \quad . \tag{43}$$

The trace is evaluated over the complete set of position states $|\, i >$ defined at each DVR grid-point (x_i, y_i)

$$Tr\,[\,''\,] = \frac{1}{\hbar}\int_{-\infty}^{\infty} dt\, \exp\left(\frac{iEt}{\hbar}\right)\int_{0+}^{\infty} dx \int_{-\infty}^{\infty} dy\, < i_f|\exp\left(\frac{i\hat{H}t}{\hbar}\right)|i_i>\Big|_{i_f=i_i=i} \quad . \tag{44}$$

In the semi-classical limit , the matrix element between $|\, i_f >$ and $|\, i_i >$ can be written as

$$< i_f|\exp\left(\frac{i\hat{H}t}{\hbar}\right)|i_i> = \frac{-i}{\hbar}\sum_{paths}\sqrt{\left|det\,\frac{\partial^2 S}{\partial i_f\,\partial i_i}\right|}\,\exp\left(i\left[\frac{S}{\hbar}-\frac{\mu\pi}{2}\right]\right) \quad , \tag{45}$$

where μ is the Maslov index, S is the action along the path connecting $|\, i_f >$ at (x_f, y_f) and $|\, i_i >$ at (x_i, y_i), and the sum is over all possible paths. Only two paths are considered; the direct and the one bounce paths. The direct path determines the action S_d along a straight line between $|\, i_f >$ and $|\, i_i >$; this term gives the majority contribution to the sum. The one bounce path determines the action S_{ob} along the straight line between $|\, \overline{i_f} >$ and $|\, i_i >$, where $|\, \overline{i_f} >$ is the reflection of the position state $|\, i_f >$ through $x = 0$. These two paths are illustrated in Figure (6).

Because the trace is evaluated only on half of the configuration space , the imposed hard wall at $x = 0$ determines the corrections to the density of states for the separate spectra. Specifically, the one bounce path effects a positive contribution to the symmetric density of states as $\mu_{ob} = 4$, while $\mu_{ob} = 2$ gives a negative contribution in the anti-symmetric case. The direct path has a Maslov index of zero. The semi-

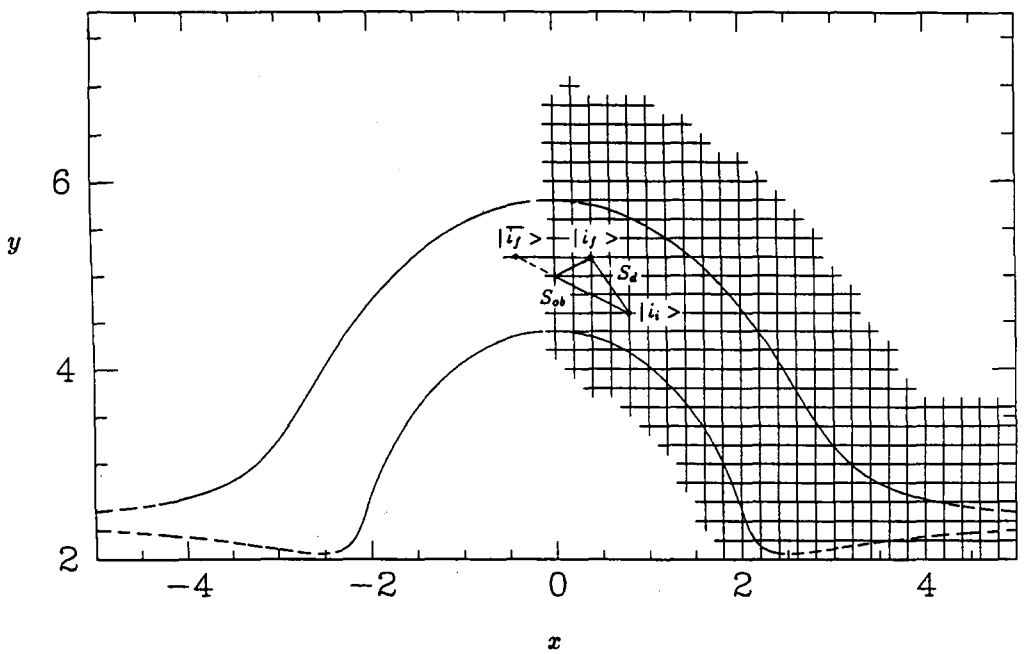

FIGURE 6. The action along the direct and one bounce paths between position states $|i_f>$ and $|i_i>$.

classical approximation to the density of states is now given by

$$\begin{aligned}\rho_{sc}(E) &= \rho_d(E) + \rho_{ob}(E) \\ &= \frac{1}{h}\int_{-\infty}^{\infty} dt\, \exp\left(\frac{iEt}{\hbar}\right) \int_{0+}^{\infty} dx \int_{-\infty}^{\infty} dy \left\{ \frac{-i}{h}\sqrt{\left|det\, \frac{\partial^2 S_d}{\partial i_f\, \partial i_i}\right|}\, \exp\left(i\left[\frac{S_d}{\hbar} - \frac{\mu_d \pi}{2}\right]\right)\right. \\ &\quad \left. + \frac{-i}{h}\sqrt{\left|det\, \frac{\partial^2 S_{ob}}{\partial i_f\, \partial i_i}\right|}\, \exp\left(i\left[\frac{S_{ob}}{\hbar} - \frac{\mu_{ob}\pi}{2}\right]\right)\right\} \quad .\end{aligned} \tag{46}$$

The action along the direct and the one bounce paths is determined using

$$\begin{aligned} S_d &= \left[\frac{(x_f - x_i)^2}{2t} + \frac{(y_f - y_i)^2}{2t} - \left(\frac{V(x_f, y_f) - V(x_i, y_i)}{2}\right) t\right]\Bigg|_{(x_f, y_f) = (x_i, y_i) = (x, y)} \quad , \\ &= -V(x, y)\, t \end{aligned} \tag{47}$$

and

$$\begin{aligned} S_{ob} &= \left[\frac{(\overline{x_f} - x_i)^2}{2t} + \frac{(\overline{y_f} - y_i)^2}{2t} - \left(\frac{V(\overline{x_f}, \overline{y_f}) - V(x_i, y_i)}{2}\right) t\right]\Bigg|_{(x_f, y_f) = (x_i, y_i) = (x, y)} \quad ; \\ &= \frac{(2x)^2}{2t} - V(x, y)\, t \end{aligned} \tag{48}$$

if it is assumed that $V(\overline{x_f}, \overline{y_f}) \simeq V(x_f, y_f)$. The determinant terms in equation (46) are evaluated for both paths to find

$$det\, \frac{\partial^2 S}{\partial i_f\, \partial i_i} = \begin{vmatrix} \frac{\partial S}{\partial x_f\, \partial x_i} & \frac{\partial S}{\partial y_f\, \partial x_i} \\ \frac{\partial S}{\partial x_f\, \partial y_i} & \frac{\partial S}{\partial y_f\, \partial y_i} \end{vmatrix} = \begin{cases} 1/t^2 & S = S_d \\ -1/t^2 & S = S_{ob} \end{cases} \quad , \tag{49}$$

and the density of states is

$$\begin{aligned}\rho_{sc}(E) &= \rho_d(E) + \rho_{ob}(E) \\ &= \frac{-i}{h^2}\int_{-\infty}^{\infty} dt\, \frac{1}{t} \int_{0+}^{\infty} dx \int_{-\infty}^{\infty} dy\ \exp\left(\frac{i[E - V(x,y)]t}{\hbar}\right) \left\{1 \pm \exp\left(\frac{2ix^2}{t\hbar}\right)\right\} \quad .\end{aligned} \tag{50}$$

From the "Tables of Fourier Transforms and Fourier Transforms of Distributions" [Ob-90], the integral over time is

$$\int_{-\infty}^{\infty} dt\, \frac{1}{t}\, \exp\left(\frac{i[E - V(x,y)]t}{\hbar}\right) = \frac{2\pi i [E - V(x,y)]_+^0}{\Gamma(1)} \quad , \tag{51}$$

where $[E - V(x,y)]_+^0 = \Theta(E - V(x,y))$ and the gamma function $\Gamma(1) = 1$. The direct term is now given by

$$\rho_d(E) = \frac{2\pi}{h^2}\int_{0+}^{\infty} dx \int_{-\infty}^{\infty} dy\, \Theta(E - V(x,y)) \quad , \tag{52}$$

which is equal to equation (38), except that the dx integration limits differ because the trace was evaluated only on half of the configuration space. The one bounce term can be expressed as

$$\rho_{ob} = (\pm 1)\,\frac{-i}{h^2}\int_{-\infty}^{\infty} dt\,\frac{1}{t}\int_{-\infty}^{\infty} dy\int_{0+}^{\infty} dx\,\exp\left(\frac{i[E-V(x,y)]t}{\hbar}\right)\exp\left(\frac{2ix^2}{t\hbar}\right) \quad . \tag{53}$$

Rapid oscillations of the factor $\exp\left(\frac{2ix^2}{t\hbar}\right)$ cancel all but small x contributions, thus $V(x,y)$ is approximated by $V(0,y)$ and the resulting Gaussian integral over x is evaluated to find

$$\rho_{ob} = (\pm 1)\,\frac{-i}{h^2}\int_{-\infty}^{\infty} dt\,\frac{1}{t}\int_{-\infty}^{\infty} dy\,\exp\left(\frac{i[E-V(0,y)]t}{\hbar}\right)\frac{1}{2}\sqrt{\frac{i\pi t\hbar}{2}} \quad . \tag{54}$$

The integration over time is performed as for the direct term, which results in

$$\rho_{ob} = (\pm 1)\,\frac{1}{2\sqrt{2}h}\int_{-\infty}^{\infty} dy\,\frac{1}{\sqrt{[E-V(0,y)]_+}} \quad . \tag{55}$$

Pulling both terms together, the density of states is now given by

$$\begin{aligned}\rho_{sc} &= \rho_d(E) + \rho_{ob}(E) \\ &= \frac{2\pi}{h^2}\int_{0+}^{\infty} dx\int_{-\infty}^{\infty} dy\,\Theta(E-V(x,y)) \pm \frac{1}{2\sqrt{2}h}\int_{-\infty}^{\infty} dy\,\frac{1}{\sqrt{[E-V(0,y)]_+}} \quad ,\end{aligned} \tag{56}$$

and the cumulative densities for the separate spectra can be determined. The number of symmetric levels with energy below the energy E is found to be

$$\begin{aligned}\overline{N_s(E)} &= \int_0^E dE'\,\rho_{sc}(E') \\ &= \int_0^E dE'\,\frac{2\pi}{h^2}\int_{0+}^{\infty} dx\int_{-\infty}^{\infty} dy\,\Theta(E-V(x,y)) + \frac{1}{2\sqrt{2}h}\int_{-\infty}^{\infty} dy\,\frac{1}{\sqrt{[E-V(0,y)]_+}} \quad .\end{aligned} \tag{57}$$

Integration over energy yields

$$\overline{N_s(E)} = \frac{2\pi}{h^2}\int_{0+}^{\infty} dx\int_{-\infty}^{\infty} dy\,[E-V(x,y)]_+ + \frac{1}{\sqrt{2}h}\int_{-\infty}^{\infty} dy\,\sqrt{[E-V(0,y)]_+} \quad , \tag{58}$$

and discretization of the integrals to the DVR grid gives

$$\overline{N_s(E)} = \frac{2\pi}{h^2}\,\Delta x\,\Delta y\left\{\sum_{i,(x_i>0)}[E-V(x_i,y_i)]_+ + \frac{h}{2\pi\sqrt{2}\Delta x}\sum_{i,(x_i=0)}\sqrt{[E-V(0,y_i)]_+}\right\} \quad . \tag{59}$$

Similar manipulations for the anti-symmetric density of states leads to

$$\overline{N_a(E)} = \frac{2\pi}{h^2}\,\Delta x\,\Delta y\left\{\sum_{i,(x_i>0)}[E-V(x_i,y_i)]_+ - \frac{h}{2\pi\sqrt{2}\Delta x}\sum_{i,(x_i=0)}\sqrt{[E-V(0,y_i)]_+}\right\} \quad . \quad (60)$$

Figures (7) and (8) show the exact cumulative densities for the symmetric and anti-symmetic spectra, along with the semi-classical approximations $\overline{N_s(E)}$ and $\overline{N_a(E)}$. The cumulative densities, $N_s(E)$ and $N_a(E)$, were determined as per equation (42), except that the sum is over either the symmetric or anti-symmetric states, respectively. The fit of the semi-classical approximation to the exact cumulative density of states is very good in both cases. The statistical properties of the flucuations $N(E)-\overline{N(E)}$ can now be investigated for the T-shaped Ar_3 energy spectrum.

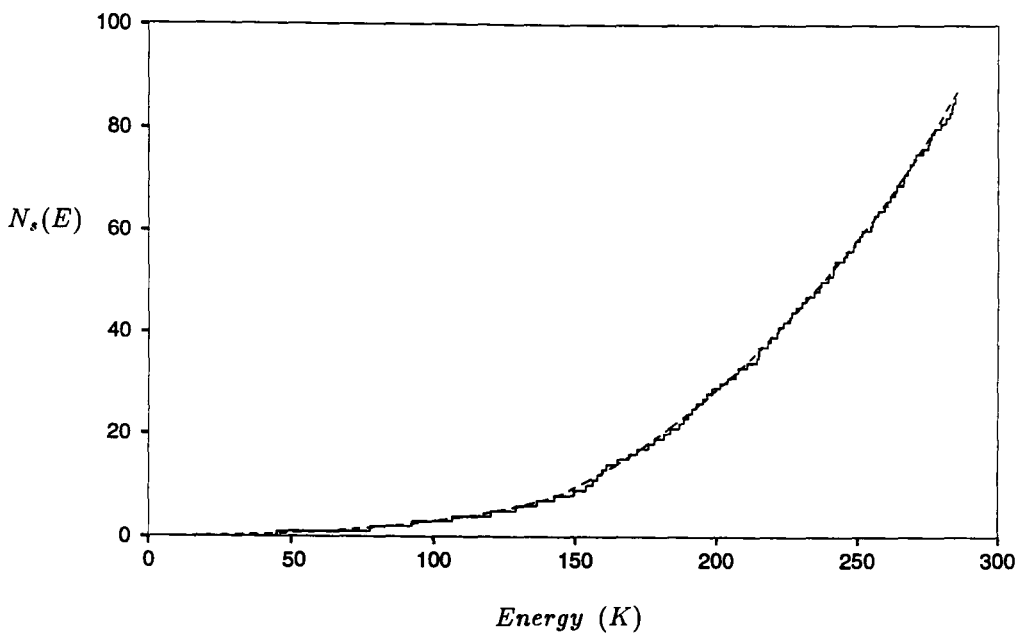

FIGURE 7. The cumulative density of states $N_s(E)$ (solid) and its semi-classical approximation $\overline{N_s(E)}$ (dashed) for the T-shaped Ar_3 symmetric energy spectrum.

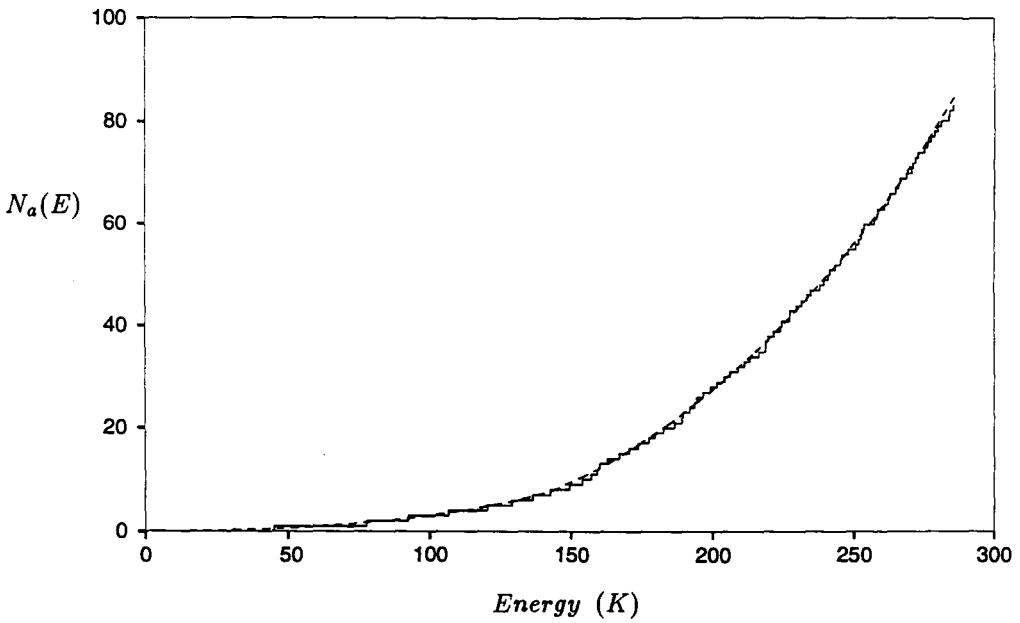

FIGURE 8. Cumulative density of states $N_a(E)$ (solid) and its semi-classical approximation $\overline{N_a(E)}$ (dashed) for the T-shaped Ar_3 anti-symmetric energy spectrum.

III.1.2 Spectral Fluctuations

The current paradigm of quantum chaos is energy spectrum statistics in accord with the Gaussian orthogonal ensemble (GOE) of random matrices. Random matrix theories, which originated in the 1950s, were constructed to describe the behaviour of slow neutron resonances in nuclear physics. The idea of a statistical description arose because of the rapid increase of level density with energy E – a detailed description of individual levels quickly becomes less meaningful. However, just when the number of levels becomes unmanageable, the distribution of levels takes on understandable statistical properties. Wigner was the first to identify the statistical properties of the energy spectrum with that of a matrix of independent Gaussian random variables. The eigenvalues of this Gaussian orthogonal ensemble of matrices have well defined statistical properties. For example, the successive level spacing distribution is given as Wigner's surmise [Wi-56],

$$P_W(s) = \frac{\pi s}{2} \exp\left(\frac{-\pi s^2}{4}\right) \quad . \tag{61}$$

The small probability of small spacings $P_W(s \to 0) \to 0$ is usually referred to in the literature as the phenomenon of level repulsion or avoided crossings. This level repulsion is in marked contrast to the frequent near degeneracies in the regular spectrum which is characterized by the Poisson distribution.

The distribution of successive scaled level spacings, $P(\Delta\overline{N})$, where

$$\Delta\overline{N} = \overline{N(E_{j+1})} - \overline{N(E_j)} \quad , \tag{62}$$

is investigated for T-shaped Ar_3. The average cumulative density $\overline{N(E)}$ is given by the semi-classical formula as described in the previous section. It is computed at a sequence of energies and interpolated at each eigenvalue E_j to determine the required $\overline{N(E_j)}$ scaled spectrum. The reduction from the energy levels E_j to the scaled energies

$N(E_j)$ removes the bias of the changing density of states. Figure (9) shows the normalized histogram of the successive level spacing distribution, along with the Wigner and Poisson functions.

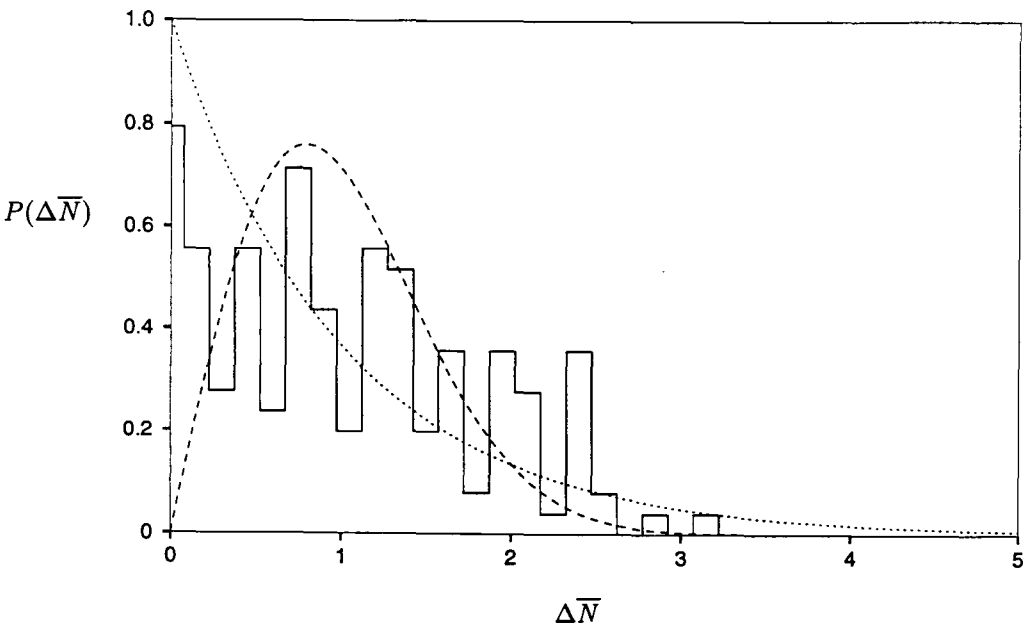

FIGURE 9. Successive level spacing distribution $P(\Delta\overline{N})$ for the T-shaped Ar_3 energy spectrum. Superimposed are the Poisson (dotted) and the Wigner (dashed) distributions.

Although the distribution does not fit either case accurately, it clearly does not resemble the Wigner function because of the non-zero density at $\Delta\overline{N} = 0$. The occurance of the near-zero values of $\Delta\overline{N}$ are a direct result of the paired eigenvalues at energies below threshold, and the approximate independence of the symmetric and anti-symmetric levels above threshold.

In addition to separating the data into symmetric and anti-symmetric subsets, the number of energy levels was increased in order to determine better converged

distributions. Even though the number of energy levels below dissociation is fixed, this number was artificially increased by decreasing $\hbar$ from the real, physical value of one [1]. That decreasing $\hbar$ results in an increase in the number of energy levels can be found by considering Weyl's formula, equation (37). For a Hamiltonian system with f degrees of freedom, the number of eigenstates with energy less than E scales as h^{-f}. The interpretation of Weyl's formula is that the volume of phase space with energy less than E supports a number of states equal to the number of volume $= h^f$ "cells" contained within the total volume. The statistics of the $P(\Delta\overline{N})$ distribution can also be improved by replacing argon with xenon. Xenon is a closed shell atom located one row below argon in the periodic table. The T-shaped trimer, Xe_3, also experiences Van der Waals' type interactions similar to those of Ar_3. However, the dissociation energy is higher than for argon, $E_{diss}(Xe_3) = 517.28K$ as compared to $E_{diss}(Ar_3) = 286.448K$; thus, the Xe_3 system has more levels below dissociation (increased mass and distance scale also contribute to the increased density of states).

Figures (10) and (11) present the results of the successive level spacing distribution for the case of T-shaped Ar_3 with $\hbar = 1/2$, and T-shaped Xe_3 with $\hbar = 1$. Again, the distributions are not of the Wigner type because of the density at $\Delta\overline{N} = 0$. In fact, the distribution in Figure (10) appears to converge towards the Poisson function. This result was unexpected because a Poisson distribution is associated with classically regular systems. However, the existence of the two distinct symmetries in the T-shaped Ar_3 Hamiltonian mimics the behaviour of a regular system. The two sets of symmetric and anti-symmetric energy levels have their own statistics, but the superposition of the independent spectra makes the resulting spectrum appear totally uncorrelated with a Poisson distribution. Any inherent symmetry in the Hamiltonian

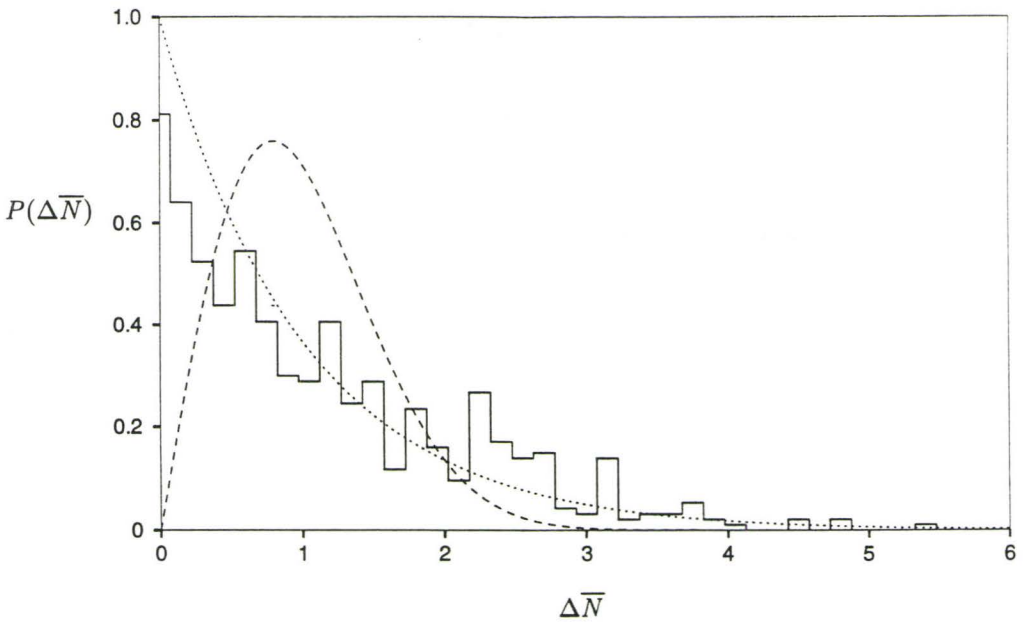

FIGURE 10. Successive level spacing distribution $P(\Delta\overline{N})$ for the T-shaped Ar_3 energy spectrum with $\hbar = 1/2$. Superimposed are the Poisson (dotted) and the Wigner (dashed) distributions.

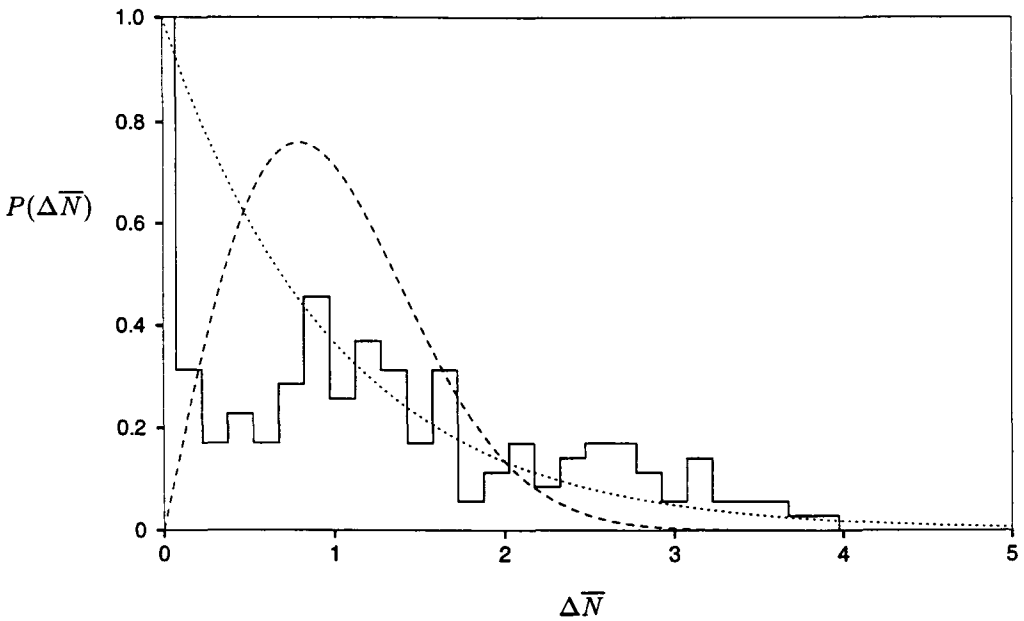

FIGURE 11. Successive level spacing distribution $P(\Delta\overline{N})$ for the T-shaped Xe_3 energy spectrum with $\hbar = 1$. Superimposed are the Poisson (dotted) and the Wigner (dashed) distributions.

must be separated before the spectral statistics are interpreted. The successive level spacing distribution for the separate spectra is shown in Figures (12) through (17). In each case, there is a much closer resemblance to the Wigner function than the Poisson. The distributions are peaked at $\Delta\overline{N} = 1$ because level crossings are avoided, *i.e.*, the levels try to stay as far apart as possible.

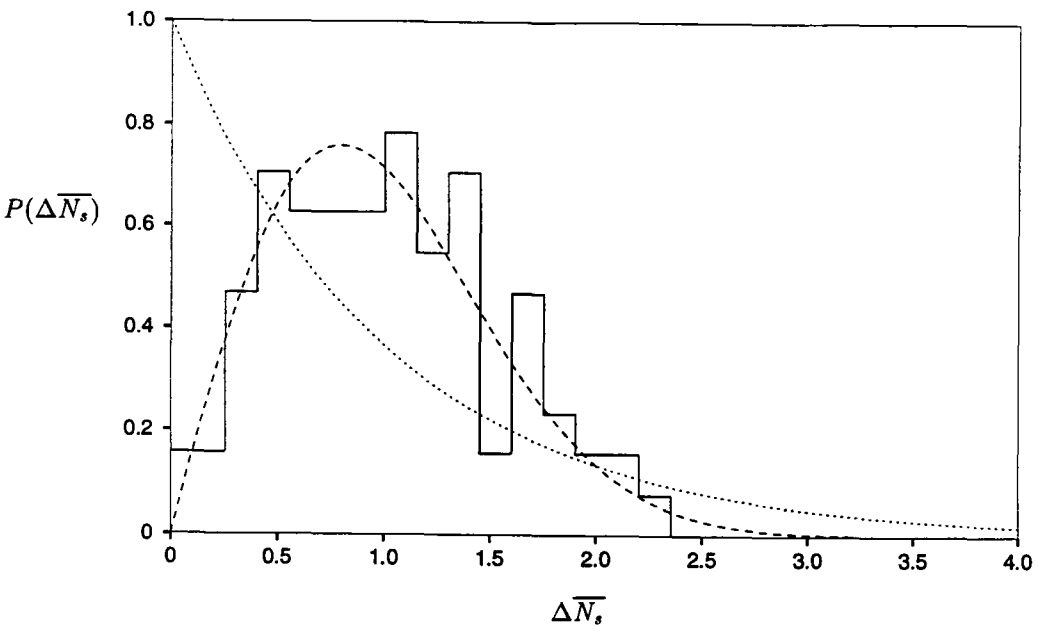

FIGURE 12. Successive level spacing distribution $P(\Delta\overline{N_s})$ for the T-shaped Ar_3 symmetric energy spectrum with $\hbar = 1$. Superimposed are the Poisson (dotted) and the Wigner (dashed) distributions.

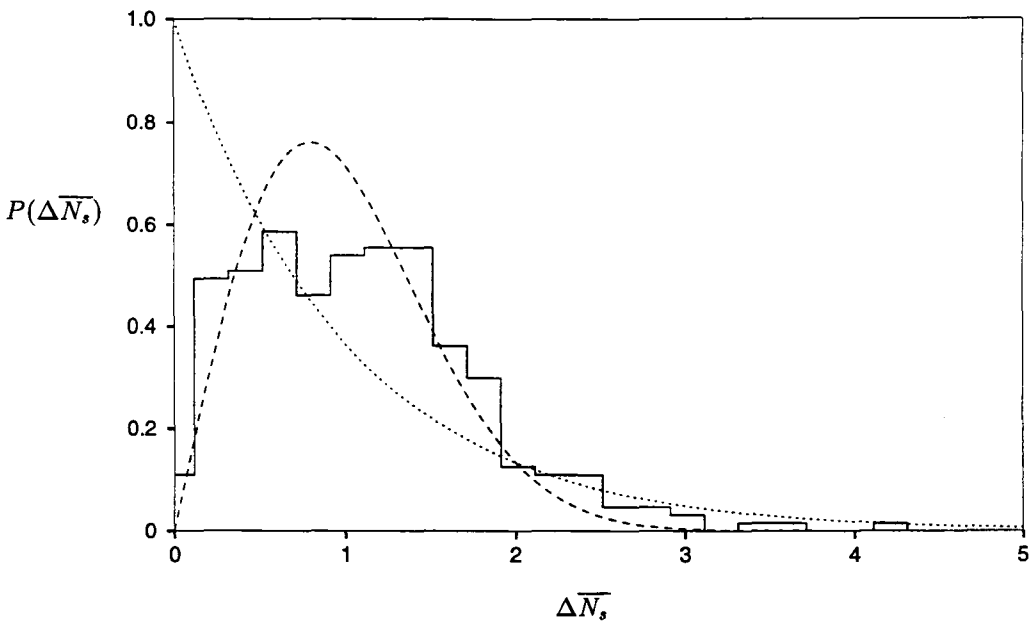

FIGURE 13. Successive level spacing distribution $P(\Delta\overline{N_s})$ for the T-shaped Ar_3 symmetric energy spectrum with $\hbar = 1/2$. Superimposed are the Poisson (dotted) and the Wigner (dashed) distributions.

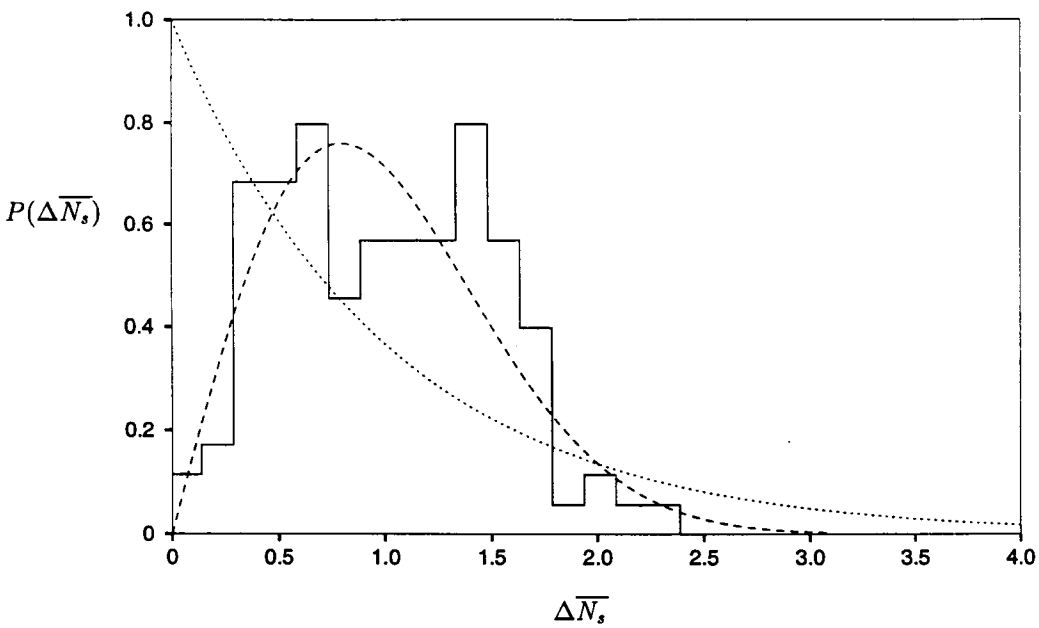

FIGURE 14. Successive level spacing distribution $P(\Delta\overline{N_s})$ for the T-shaped Xe_3 symmetric energy spectrum with $\hbar = 1$. Superimposed are the Poisson (dotted) and the Wigner (dashed) distributions.

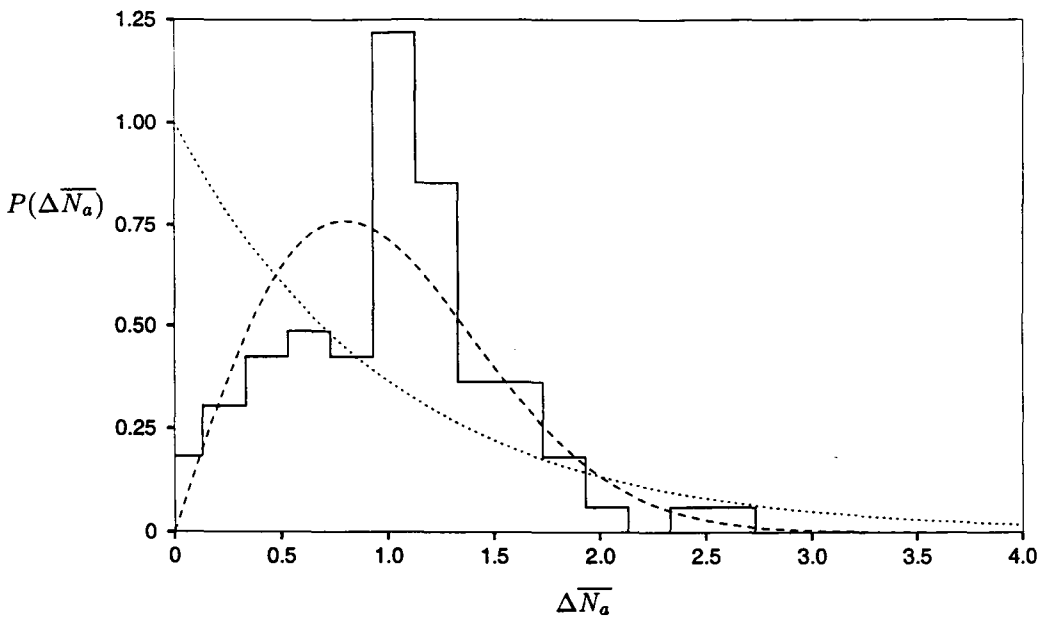

FIGURE 15. Successive level spacing distribution $P(\Delta\overline{N_a})$ for the T-shaped Ar_3 anti-symmetric energy spectrum with $\hbar = 1$. Superimposed are the Poisson (dotted) and the Wigner (dashed) distributions.

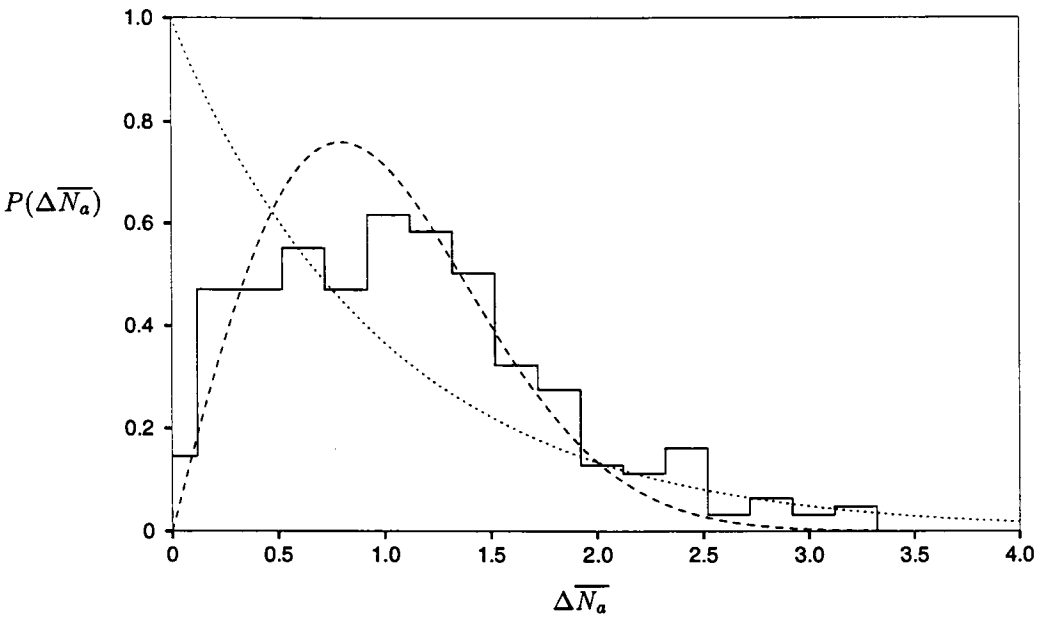

FIGURE 16. Successive level spacing distribution $P(\Delta\overline{N_a})$ for the T-shaped Ar_3 anti-symmetric energy spectrum with $\hbar = 1/2$. Superimposed are the Poisson (dotted) and the Wigner (dashed) distributions.

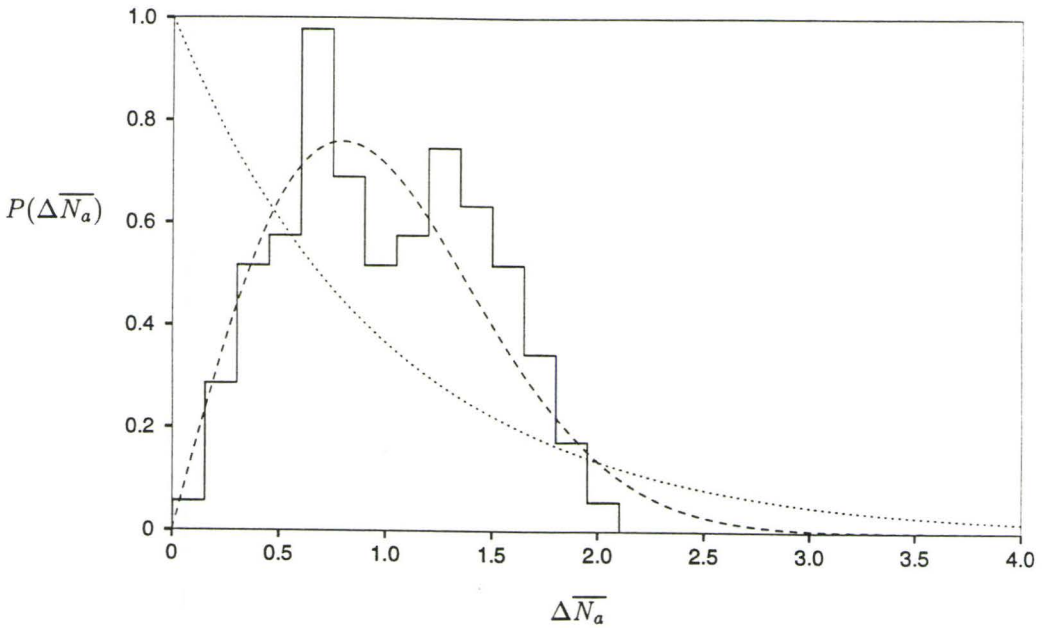

FIGURE 17. Successive level spacing distribution $P(\Delta\overline{N_a})$ for the T-shaped Xe_3 anti-symmetric energy spectrum with $\hbar = 1$. Superimposed are the Poisson (dotted) and the Wigner (dashed) distributions.

Large scale calculations of energy levels were carried out for the stadium and the billiard by Bohigas, Giannoni and Schmit [BGS-84], and for the hydrogen atom in a magnetic field by Delande and Gay [DG-86]. The agreement with predictions of the GOE of random matrices is excellent. This led to the speculation that the GOE statistics identify a universal property of the energy levels in a classically chaotic system. While numerical studies support this conjecture, a theoretical justification has yet to appear. An explanation has been offered by Berry [Be-85] where an explicit statement about the classical behaviour is used and then transformed into a statistical proposition. Nevertheless, the successive level spacing distribution is used as an indication that T-shaped Ar_3 is chaotic for all accessible energies.

III.2 Energy Eigenfunction Statistical Properties

Characteristic statistical properties have also been observed in the stationary and time-dependent wavefunctions of quantum analogues to classically chaotic systems. The features of the wavefunction appear qualitatively different in the semiclassical limit for states corresponding to regular or chaotic classical dynamics. Berry [Be-77] conjectured that the eigenstates associated with a chaotic energy spectrum are Gaussian random functions of position. All statistical properties of a Gaussian random function are determined by the spatial distribution function and the spatial pair-correlation function.

III.2.1 Spatial Distribution of Energy Eigenfunctions

The main property of a Gaussian random function $\varphi(x)$ is that the distribution function of its amplitude is Gaussian,

$$P_D(\varphi(x)) = \sqrt{\frac{1}{2\pi\sigma^2}} \exp\left(-\frac{\varphi(x)^2}{2\sigma^2}\right) \quad , \tag{63}$$

where σ^2 is the variance of $\varphi(x)$. This result was verified by numerical studies [SG-84, AS-91] of chaotic eigenfunctions which show that the spatial distribution function is Gaussian, while regular eigenfunctions find non-Gaussian distributions. For a bound system the variance is given by,

$$\sigma^2 = \frac{1}{2A_j} \quad , \tag{64}$$

where A_j is the area of the classically allowed region in configuration space with $x > 0$ associated with the j^{th} energy eigenstate. The spatial distribution function is now expessed as

$$P_D(\varphi(x)) = \sqrt{\frac{A_j}{\pi}} \exp\left(-A_j\,(\varphi(x))^2\right) \quad . \tag{65}$$

The spatial distribution of the energy eigenfunctions was determined for the classically chaotic T-shaped Ar_3 system. The classically allowed region of configura-

tion space for an eigenfunction $\psi^j(x,y)$ with associated energy E_j is given by

$$A_j = \int_{0+}^{\infty} dx \int_{-\infty}^{\infty} dy\, \Theta(E_j - V(x,y)) \quad ; \tag{66}$$

discretizing to the DVR grid finds

$$A_j = \Delta x\, \Delta y \left\{ \sum_{i,(x_i>0)} [E_j - V(x_i,y_i)]_+^0 + \sum_{i,(x_i=0)} \frac{1}{2} [E_j - V(x_i,y_i)]_+^0 \right\} \quad . \tag{67}$$

Figures (18) and (19) show spatial distribition functions $P_D(\psi^j)$ for symmetric and anti-symmetric T-shaped Ar_3 energy eigenfunctions. The spatial distribution functions are well-approximated by Gaussians in each case.

III.2.2 Spatial Correlation of Energy Eigenfunctions

The Gaussian distribution of amplitudes is a trivial integral property of a Gaussian random or "stochastic" function. More convincing evidence of characteristic statistical properties is found in the spatial pair-correlation function. In general, the pair-correlation function is defined as

$$C[\psi,\psi](l) = \frac{1}{K} \int d\vec{r}\; \psi(\vec{r} - \tfrac{l}{2})\, \psi(\vec{r} + \tfrac{l}{2}) \quad . \tag{68}$$

Here, K is a normalization constant and l is the length of the spatial correlation. The size of the integration area should be much larger than l. This correlation is a reflection of the pattern of oscillations of $\psi(\vec{r})$. If ψ is a Gaussian random function of position then an average (integral) over the area is equivalent to an average over the ensemble of ψ values. Berry [Be-77] predicted that the spatial pair-correlation function of an ensemble average of random wavefunctions is given by

$$C[\psi,\psi](l) = \overline{\psi(\vec{r} - \tfrac{l}{2})\, \psi(\vec{r} + \tfrac{l}{2})} = \sigma^2\, J_0 \left[\sqrt{2(E - V(\vec{r})}\, \frac{l}{\hbar} \right] \quad . \tag{69}$$

This prediction can be verified by extracting the argument of the Bessel function for different lengths l and the averages $\overline{\psi(\vec{r} - \frac{l}{2})\, \psi(\vec{r} + \frac{l}{2})}$ and comparing to a zeroth-order Bessel function.

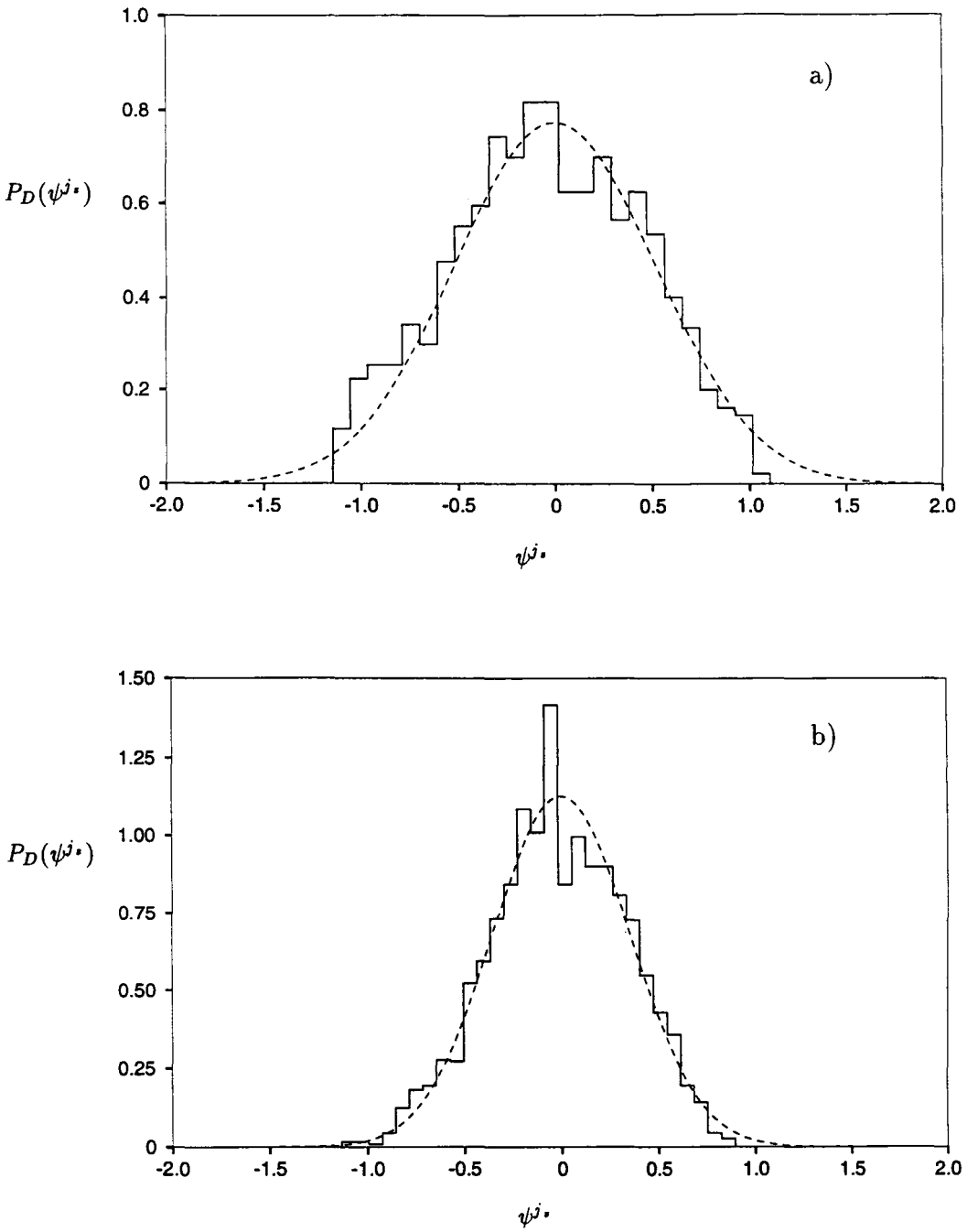

FIGURE 18. Spatial distribution functions $P_D(\psi^{j_s})$ for the T-shaped Ar_3 symmetric energy eigenfuntions; *a*) $j_s = 12$ $(E_{j_s} = 158.02K)$, *b*) $j_s = 50$ $(E_{j_s} = 237.46K)$.

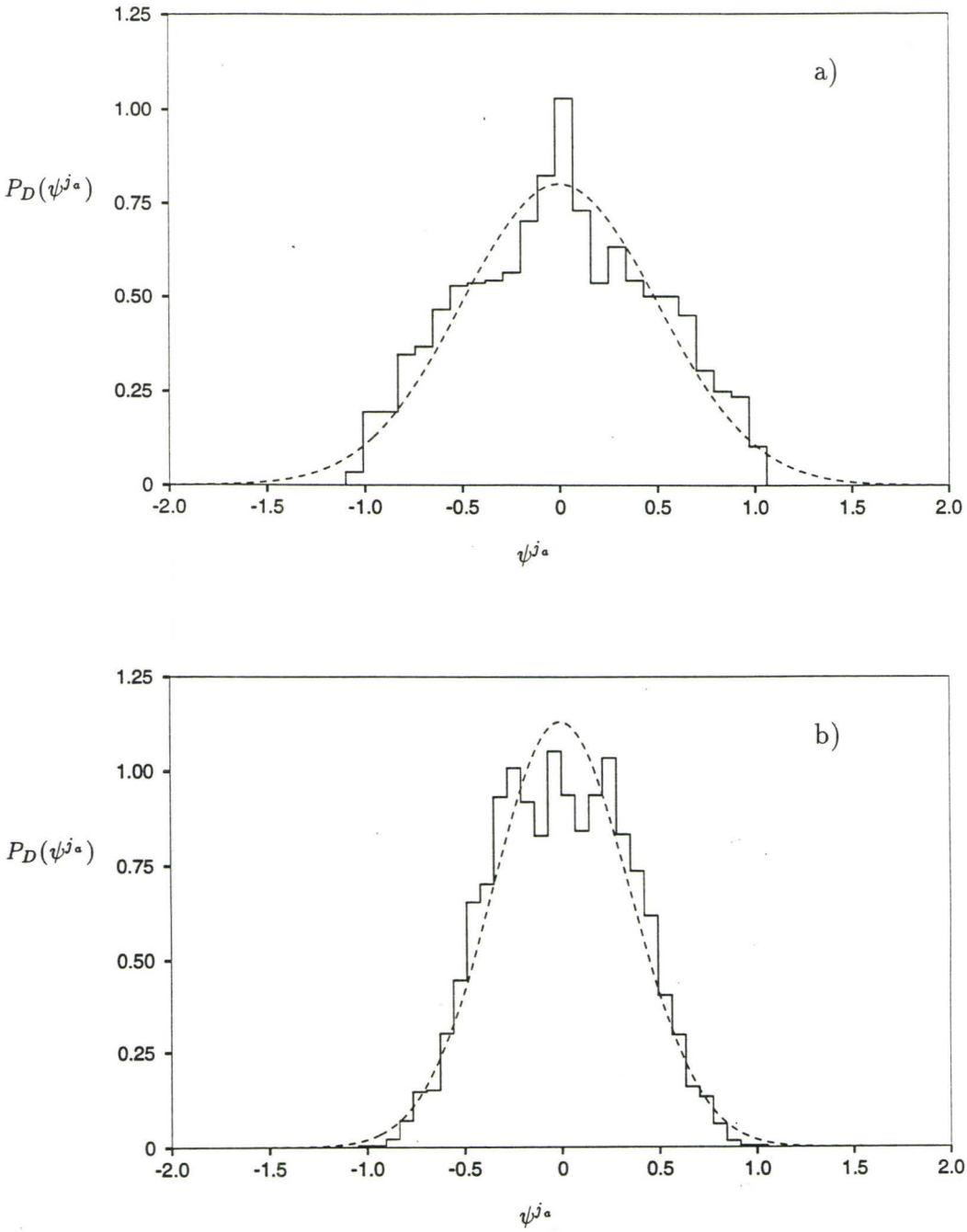

FIGURE 19. Spatial distribution functions $P_D(\psi^{j_a})$ for the T-shaped Ar_3 anti-symmetric energy eigenfunctions; *a*) $j_a = 14$ ($E_{j_a} = 163.01K$), *b*) $j_a = 50$ ($E_{j_a} = 240.94K$).

In terms of the DVR grid, the spatial pair-correlation function is expressed as

$$C[\psi^j, \psi^j](r'_{ik}) = \frac{1}{2A_j} J_0 \left[\sqrt{2(E^j - V(r^\circ_{ik})} \, \frac{r'_{ik}}{\hbar} \right] \quad , \tag{70}$$

where r°_{ik} is the mid-point and

$$r'_{ik} = \sqrt{(x_i - x_k)^2 + (y_i - y_k)^2} \quad , \tag{71}$$

is the distance between the grid-points $i = (x_i, y_i)$ and $k = (x_k, y_k)$. Figures (20) to (22) show the numerical results of the spatial pair-correlation function for a range of T-shaped Ar_3 symmetric and anti-symmetric energy eigenfunctions. The agreement of the simple $J_0(z)$ formula with the chaotic eigenfunctions is quite good for small z.

Similar calculations were done by Lan, Shushin and Wardlaw [LSW-92] on time-dependent wavefunctions for classically chaotic bound and scattering systems with two degrees of freedom. The spatial flucuations of the wavefunctions were shown to be reproduced quite accurately by the random plane-wave superposition approximation. While this approximation lends a theoretical justification for the statistical properties, it is believed to break down at large correlation lengths. However, the spatial pair-correlation function is used as a qualitative indicator that quantum manifestations of classical chaos are evident in the T-shaped Ar_3 energy eigenfunctions.

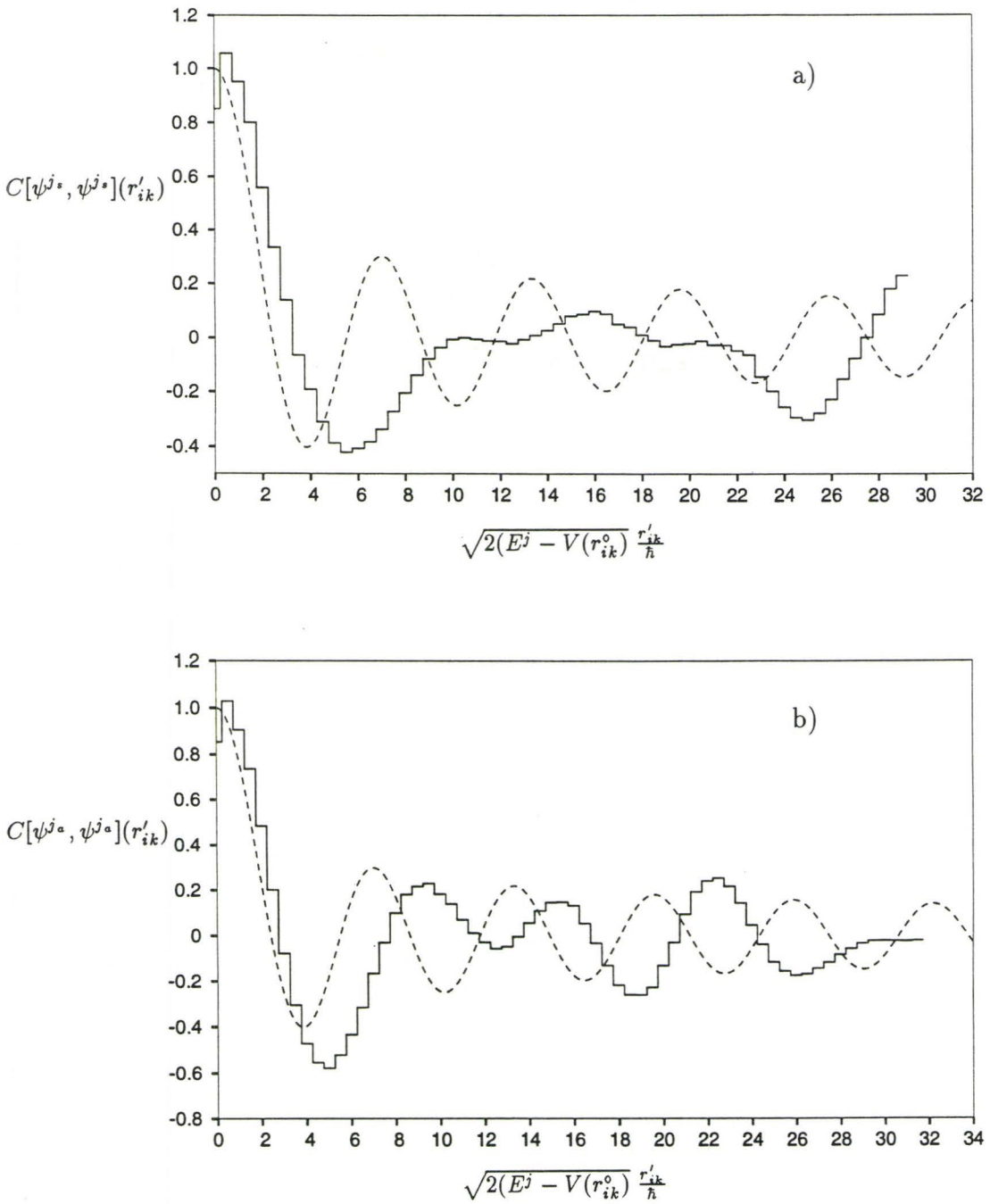

FIGURE 20. Spatial pair-correlation functions $C[\psi^j, \psi^j](r'_{ik})$ for the near threshold T-shaped Ar_3 symmetric energy eigenfunction; a) $j_s = 12$ $(E_{j_s} = 158.02K)$, and anti-symmetric eigenfunction, b) $j_a = 14$ $(E_{j_a} = 163.01K)$.

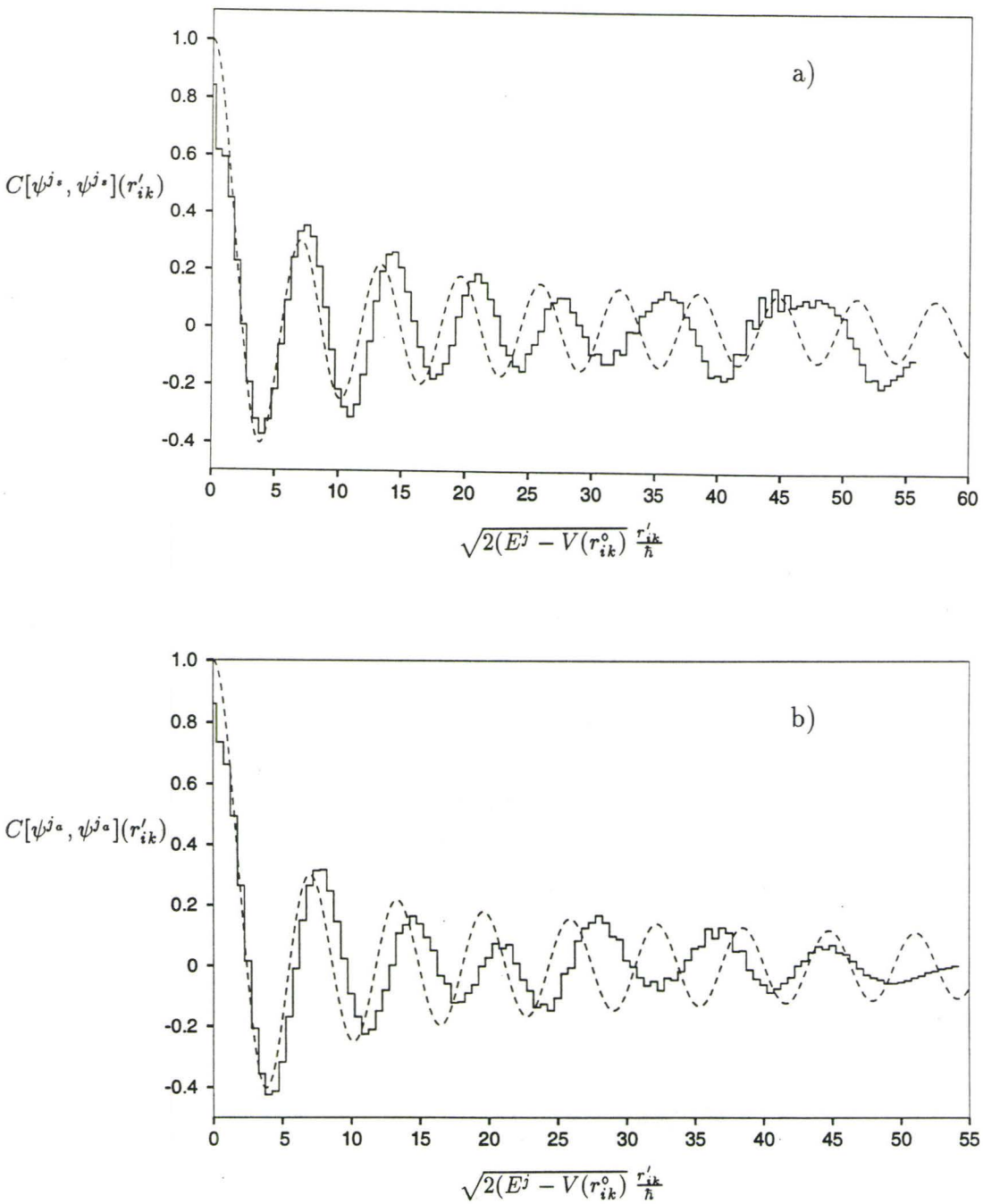

FIGURE 21. Spatial pair-correlation functions $C[\psi^j, \psi^j](r'_{ik})$ for the above threshold T-shaped Ar_3 symmetric energy eigenfunction; a) $j_s = 32$ $(E_{j_s} = 207.50K)$, and anti-symmetric eigenfunction, b) $j_a = 30$ $(E_{j_a} = 204.13K)$.

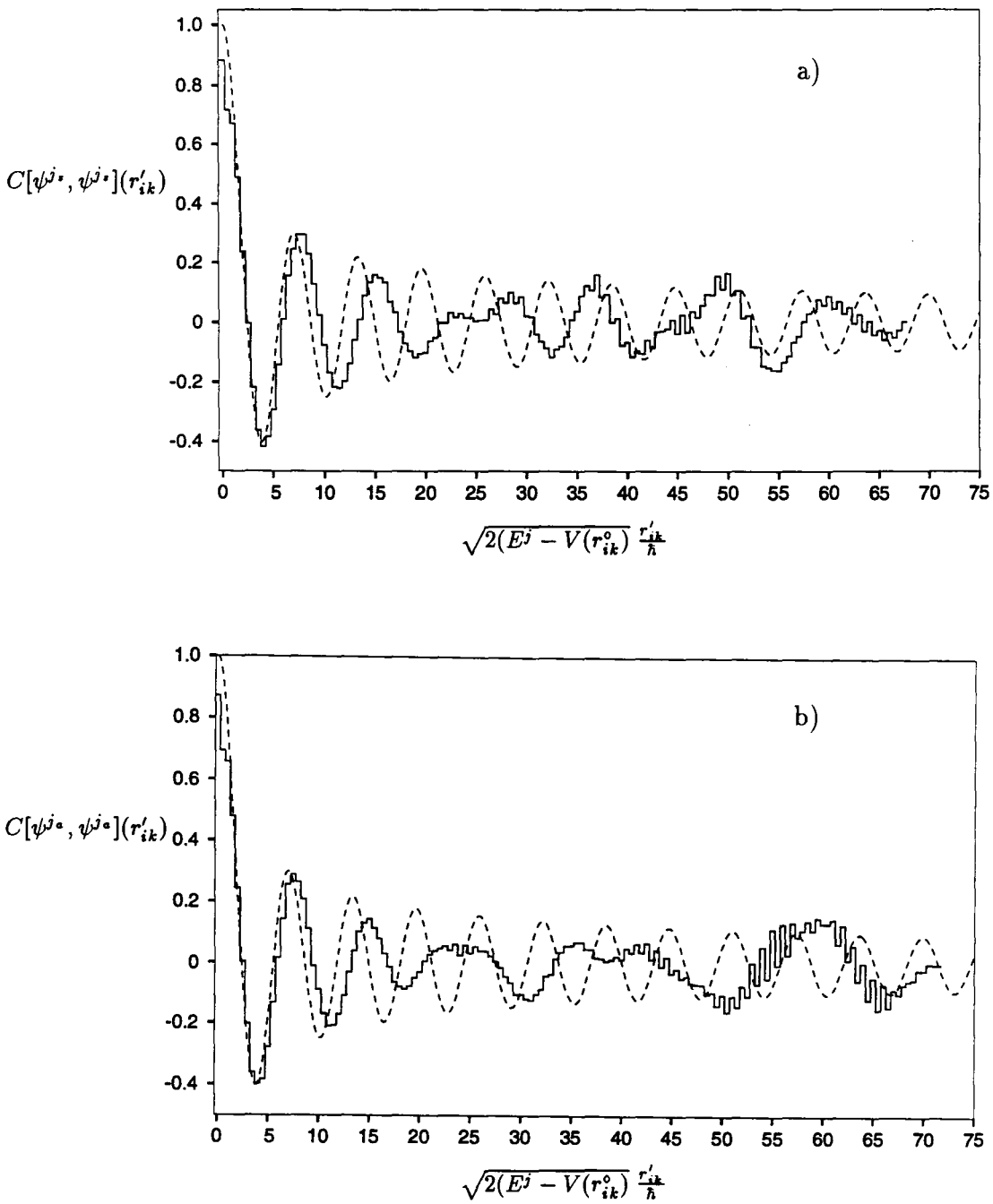

FIGURE 22. Spatial pair-correlation functions $C[\psi^j, \psi^j](r'_{ik})$ for the above threshold T-shaped Ar_3 symmetric energy eigenfunction; a) $j_s = 50$ $(E_{j_s} = 237.46K)$, and anti-symmetric eigenfunction, b) $j_a = 55$ $(E_{j_a} = 248.08K)$.

PART IV

T-Shaped Ar_3 Inversion Dynamics

PART IV

T-Shaped Ar_3 Inversion Dynamics

Molecular dynamics is concerned with the internal motion of electrons and nuclei within reacting molecules. The most widely used method for describing the dynamics of the nuclei is the classical trajectory approach. In this treatment, the motion of the nuclei on the Born-Oppenheimer potential energy surface is solved by using Newton's equations of motion. Quantum effects can be important in even very simple chemical processes – ideally, dynamics should be given a quantum mechanical description. Full scale quantum mechanical molecular dynamics requires the manipulation of large Hamiltonian matrices. New methodologies, like the discrete variable representation, make quantum molecular dynamics computations much more feasible. However, it is the aim of this work to introduce a statistical means of obtaining dynamical observables, circumventing the usually time and memory intensive matrix diagonalization. This statistical treatment utilizes the characteristic statistical properties of the energy eigenvalues and eigenfunctions, which can presumably be predicted once the corresponding classical dynamics is known.

IV.1 Survival Probability

The dynamical process of interest is the isomerization reaction exhibited by the T-shaped Ar_3 molecule (Figure 1). This process can be characterized through the survival probability, $C(t)$, which is expressed as

$$C(t) = \frac{Tr\left[\exp\left(-\beta\hat{H}\right)\hat{h}(x)\,\hat{\varrho}_x(t)\right]}{Tr\left[\exp\left(-\beta\hat{H}\right)\hat{h}(x)\right]} \quad . \tag{72}$$

Here, $\beta = \frac{1}{k_B T}$ incorporates the specification of an initial temperature T, and $\hat{h}(x)$ is a Heaviside (step) function. The time-evolved projection operator $\hat{\varrho}_x(t)$ is defined as

$$\hat{\varrho}_x(t) = \exp\left(\frac{-i\hat{H}t}{\hbar}\right)\hat{h}(x)\exp\left(\frac{i\hat{H}t^*}{\hbar}\right) \quad ; \tag{73}$$

it projects onto all states at time t that have a positive x-coordinate in configuration space. The quantity in the denominator of equation (72) is the partition function, Q

$$Q = Tr\left[\exp\left(-\beta\hat{H}\right)\hat{h}(x)\right] \quad . \tag{74}$$

It is customary [MST-83] to recast equation (72) in a more symmetrical form which permits identification of temperature as an imaginary time. Specifically, from the commutation properties of the two operators, $\hat{\varrho}_x(t)$ and $\exp\left(-\beta\hat{H}\right)$, then the survival probability can be written as

$$C(t) = \frac{Tr\left[\hat{h}(x)\exp\left(-\frac{\beta\hat{H}}{2}\right)\hat{\varrho}_x(t)\exp\left(-\frac{\beta\hat{H}}{2}\right)\right]}{Q} \quad , \tag{75}$$

which leads to,

$$C(t) = \frac{Tr\left[\hat{h}(x)\exp\left(\frac{-i\hat{H}t_c}{\hbar}\right)\hat{h}(x)\exp\left(\frac{i\hat{H}t_c^*}{\hbar}\right)\right]}{Q} \quad , \tag{76}$$

where t_c is the complex time given by

$$t_c = t - \frac{i\hbar\beta}{2} \quad . \tag{77}$$

When the trace is evaluated in the energy representation, matrix elements arise between two eigenstates ψ^j and ψ^k of the projection operator $\hat{h}(x)$ as

$$< \psi^j \,|\, \hat{h}(x) \,|\, \psi^k > = \int_{-\infty}^{\infty} dx\, dy\, \psi^j(x,y)\,\hat{h}(x)\,\psi^k(x,y) = \int_{0+}^{\infty} dx \int_{-\infty}^{\infty} dy\, \psi^j(x,y)\,\psi^k(x,y) \quad , \tag{78}$$

which is a result of the definition of the projection operator

$$\hat{h}(x)\,\psi^j(x,y) = \begin{cases} \psi^j(x,y) & x > 0 \\ 0 & x < 0 \end{cases} \quad . \tag{79}$$

The matrix element is the projection of the states onto $x > 0$ configuration space. The properties of the projection matrix are key to the development of a statistical model for the T-shaped Ar_3 survival probability.

IV.1.2 Properties of the T-Shaped Ar_3 Projection Matrix

The symmetry of the T-shaped Ar_3 energy eigenfunctions $\{\psi^j\}$, where $j = j_s$ or $j = j_a$, is used to recast their orthogonality in terms of the matrix elements of the projection operator. Specifically, the normalization condition

$$\delta_{j,k} = \int_{-\infty}^{\infty} dx \int_{-\infty}^{\infty} dy\, \psi^j(x,y)\, \psi^k(x,y) \quad , \tag{80}$$

can be expanded as

$$\delta_{j,k} = \int_{-\infty}^{0^-} dx \int_{-\infty}^{\infty} dy\, \psi^j(x,y)\, \psi^k(x,y) + \int_{0+}^{\infty} dx \int_{-\infty}^{\infty} dy\, \psi^j(x,y)\, \psi^k(x,y) \quad . \tag{81}$$

From the definition of the projection operator in equation (79), and the properties of the T-shaped Ar_3 energy eigenfunctions

$$\psi^j(x,y) = \psi^j(-x,y) \qquad j = j_s \quad , \tag{82}$$

$$\psi^j(x,y) = -\psi^j(-x,y) \qquad j = j_a \quad , \tag{83}$$

then equation (81) can be expressed as

$$\begin{aligned} \delta_{j,k} &= (1+\kappa) \int_{-\infty}^{\infty} dx \int_{-\infty}^{\infty} dy\, \psi^j(x,y)\, \hat{h}(x)\, \psi^k(x,y) \\ &= (1+\kappa) < \psi^j(x,y) \,|\, \hat{h}(x) \,|\, \psi^k(x,y) > \quad . \end{aligned} \tag{84}$$

The constant κ has the values

$$\kappa = \begin{cases} 1 & \psi^j \text{ and } \psi^k \text{ have the same symmetry; } e.g.,\ j = j_s, k = k_s \\ -1 & \psi^j \text{ and } \psi^k \text{ have the opposite symmetry; } e.g.,\ j = j_s, k = k_a \end{cases} \quad . \tag{85}$$

Setting $\kappa = 1$ in equation (84) shows that $2\hat{h}(x)$ is the identity operator in the space of same symmetry matrix elements. The isomerization dynamics is therefore manifest only in the opposite symmetry matrix elements which are denoted by

$$h_{j_s,k_a} = < \psi^{j_s}(x,y) \,|\, \hat{h}(x) \,|\, \psi^{k_a}(x,y) > \quad . \tag{86}$$

The symmetry of the full matrix determines the other opposite matrix elements, *i.e.*,

$$< \psi^{j_s}(x,y) \,|\, \hat{h}(x) \,|\, \psi^{k_a}(x,y) > = < \psi^{k_a}(x,y) \,|\, \hat{h}(x) \,|\, \psi^{j_s}(x,y) > \quad . \tag{87}$$

Equation (84) determines a "scaled" normalization property for each of the four blocks of the projection matrix denoted by $h_{j,k}$ where $j = j_s$, or j_a and $k = k_s$, or k_a. In the space of the same symmetry elements, $\{\sqrt{2}\,\psi^j(x,y)\}$ is a complete orthonormal basis set on $x > 0$; this is seen by expressing equation (84) as

$$\delta_{j,k} = \int_{0+}^{\infty} dx \int_{-\infty}^{\infty} dy \, \sqrt{2}\,\psi^j(x,y) \, \sqrt{2}\,\psi^k(x,y) \quad . \tag{88}$$

Therefore, an arbitrary anti-symmetric state $\psi^{k_a}(x,y)$ can be expanded in terms of the set $\{\sqrt{2}\,\psi^{j_s}(x,y)\}$ as

$$\psi^{k_a}(x,y) = \sum_{k_s} a_{k_s} \, \sqrt{2}\,\psi^{k_s}(x,y) \quad , \tag{89}$$

where the expansion co-effecients a_{k_s} are determined by multiplying the above equation by $\sqrt{2}\,\psi^{j_s}(x,y)$ and intregrating the result over $x > 0$ to find

$$a_{j_s} = \sqrt{2} \int_{0+}^{\infty} dx \int_{-\infty}^{\infty} dy \, \psi^{j_s}(x,y) \, \psi^{k_a}(x,y) = \sqrt{2}\, h_{j_s,k_a} \quad . \tag{90}$$

The scaled normalization property arises from the square of equation (89); explicity,

$$\psi^{j_a}(x,y) \, \psi^{k_a}(x,y) = \left(\sum_{j_s} a_{j_s} \, \sqrt{2}\,\psi^{j_s}(x,y) \right) \left(\sum_{k_s} a_{k_s} \, \sqrt{2}\,\psi^{k_s}(x,y) \right) \quad ; \tag{91}$$

integrating over $x > 0$ and using the identity in equation (88), the sum of the squares of the expansion coeffecients is

$$\sum_{j_s} (a_{j_s})^2 = \frac{1}{2} \quad . \tag{92}$$

Since equation (90) relates a_{j_s} to the projection matrix element, then the normalization property of the block h_{j_s,k_a} is given by the sum over the rows j_s (or columns k_a)

$$\sum_{j_s} (h_{j_s,k_a})^2 = \frac{1}{4} \quad ; \tag{93}$$

in general, this property of the sum of the squares of the projection matrix elements along any row or column can be shown to the true for each of the four blocks of the projection matrix.

Another expression for the projection matrix element h_{j_s,k_a} can be determined from the energy splitting, $E_{k_a} - E_{j_s}$. Consider the time independent Schrödinger equation

$$\hat{H}\psi^{j} = E_j\psi^{j} \quad ; \tag{94}$$

the energy splitting between the symmetric state ψ^{j_s} and the anti-symmetric state ψ^{k_a} can be derived as follows: the equations

$$\hat{H}\psi^{j_s} = E_{j_s}\psi^{j_s} \quad , \tag{95}$$

$$\hat{H}\psi^{k_a} = E_{k_a}\psi^{k_a} \quad ; \tag{96}$$

are multiplied on the left by the opposite symmetry wavefunction and then subtracted to give

$$\begin{aligned} \psi^{j_s}\hat{H}\psi^{k_a} - \psi^{k_a}\hat{H}\psi^{j_s} &= \psi^{j_s}E_{k_a}\psi^{k_a} - \psi^{k_a}E_{j_s}\psi^{j_s} \\ &= (E_{k_a} - E_{j_s})\,\psi^{j_s}\psi^{k_a} \quad . \end{aligned} \tag{97}$$

Integrating over the positive x-coordinate region of configuration space determines the expression

$$\begin{aligned} \int_{0+}^{\infty} dx \int_{-\infty}^{\infty} dy \left\{\psi^{j_s}\hat{H}\psi^{k_a} - \psi^{k_a}\hat{H}\psi^{j_s}\right\} &= (E_{k_a} - E_{j_s}) \int_{0+}^{\infty} dx \int_{-\infty}^{\infty} dy\, \psi^{j_s}\psi^{k_a} \\ &= (E_{k_a} - E_{j_s}) < \psi^{j_s} \,|\, \hat{h}(x) \,|\, \psi^{k_a} > \quad . \end{aligned} \tag{98}$$

The projection matrix element can be evaluated explicity by substituting the form of the Hamiltonian given in equation (1), this determines the expression

$$\begin{aligned} (E_{k_a} - E_{j_s}) < \psi^{j_s} \,|\, \hat{h}(x) \,|\, \psi^{k_a} > = \int_{0+}^{\infty} dx \int_{-\infty}^{\infty} dy \Bigg\{ & \psi^{j_s} \left[\frac{\hat{p}_x^2}{2} + \frac{\hat{p}_y^2}{2} + \hat{V}(x,y) \right] \psi^{k_a} \\ & - \psi^{k_a} \left[\frac{\hat{p}_x^2}{2} + \frac{\hat{p}_y^2}{2} + \hat{V}(x,y) \right] \psi^{j_s} \Bigg\} \quad . \end{aligned} \tag{99}$$

The potential energy terms cancel, leaving matrix elements of the kinetic energy operators

$$\hat{p}_x^2 = -\hbar^2 \frac{\partial^2}{\partial x^2} \qquad \hat{p}_y^2 = -\hbar^2 \frac{\partial^2}{\partial y^2} \quad , \tag{100}$$

which can be written as

$$(E_{k_a} - E_{j_s}) < \psi^{j_s} | \hat{h}(x) | \psi^{k_a} > = -\frac{\hbar^2}{2} \int_{0+}^{\infty} dx \int_{-\infty}^{\infty} dy \, \{\psi^{j_s} \nabla^2 \psi^{k_a} - \psi^{k_a} \nabla^2 \psi^{j_s}\} \quad , \tag{101}$$

where ∇^2 is the Laplacian. The final form of the equation is given by

$$(E_{k_a} - E_{j_s}) < \psi^{j_s} | \hat{h}(x) | \psi^{k_a} > = \frac{\hbar^2}{2} \int_{\Re} dy \left\{ \left(\psi^{j_s} \frac{\partial}{\partial x} \psi^{k_a} \right)_{x=0} + \left(\psi^{k_a} \frac{\partial}{\partial x} \psi^{j_s} \right)_{x=0} \right\} \quad ; \tag{102}$$

this result is a consequence of applying the divergence theorem – the full details are presented in Appendix B. Because of the properties of the T-shaped Ar_3 energy eigenfunctions in equations (82) and (83), then $\psi^{k_a}(x,y)_{x=0} = 0$ and $(\frac{\partial}{\partial x} \psi^{j_s}(x,y))_{x=0} = 0$. The latter result arises because the symmetric eigenfunction has an extremum at $x = 0$. Consequently, the second term in equation (102) vanishes leaving the expression

$$(E_{k_a} - E_{j_s}) < \psi^{j_s} | \hat{h}(x) | \psi^{k_a} > = \frac{\hbar^2}{2} \int_{\Re} dy \left(\psi^{j_s} \frac{\partial}{\partial x} \psi^{k_a} \right)_{x=0} \quad , \tag{103}$$

which relates the projection matrix element h_{j_s,k_a} to the associated energy splitting and boundary surface overlap integral.

IV.2. T-Shaped Ar_3 Survival Probability

An expression for the T-shaped Ar_3 survival probability can be determined by evaluating the trace in equation (76) over the set of T-shaped Ar_3 energy eigenfunctions, $\{\psi^j\}$. A quantum mechanical trace is evaluated by inserting a complete set of orthonormal functions for each operator; for example,

$$Tr\left[\hat{A}\hat{B}\right] = \sum_{i,j} < \psi^i | \hat{A} | \psi^j > < \psi^j | \hat{B} | \psi^i > \quad , \tag{104}$$

where

$$\sum_i |\psi^i><\psi^j| = \delta_{i,j} \quad , \tag{105}$$

is a complete set. The resulting matrix elements are easily evaluated using the fact that

$$<\psi^j|\exp\left(\frac{-i\hat{H}t_c}{\hbar}\right)|\psi^k> = \exp\left(\frac{-iE_kt_c}{\hbar}\right)<\psi^j|\psi^k> = \exp\left(\frac{-iE_kt_c}{\hbar}\right)\delta_{j,k} \quad , \tag{106}$$

and

$$<\psi^k|\hat{h}(x)|\psi^j><\psi^j|\hat{h}(x)|\psi^k> = |<\psi^j|\hat{h}(x)|\psi^k>|^2 \quad , \tag{107}$$

such that the survival probability is given by

$$C(t) = \frac{\sum_{j,k}\exp\left(\frac{-iE_kt_c}{\hbar}\right)\exp\left(\frac{iE_jt_c^*}{\hbar}\right)|<\psi^j|\hat{h}(x)|\psi^k>|^2}{\sum_j\exp(-\beta E_j)<\psi^j|\hat{h}(x)|\psi^j>} \quad . \tag{108}$$

The sum in the numerator is expanded, and from the cosine identity

$$\cos(x) = \frac{\exp(ix)+\exp(-ix)}{2} \quad , \tag{109}$$

then the final form of the expression is

$$\begin{aligned} C(t) = \frac{1}{Q}\Bigg\{&\sum_j\exp(-\beta E_j)|<\psi^j|\hat{h}(x)|\psi^j>|^2 \\ &+\sum_{j<k}2\exp\left(-\frac{\beta(E_j+E_k)}{2}\right)\cos\left[\frac{(E_j-E_k)t}{\hbar}\right]|<\psi^j|\hat{h}(x)|\psi^k>|^2\Bigg\} \quad , \end{aligned} \tag{110}$$

where the partition function

$$Q = \sum_j\exp(-\beta E_j)<\psi^j|\hat{h}(x)|\psi^j> \quad . \tag{111}$$

Along with the T-shaped Ar_3 energy eigenvalues $\{E_j\}$, an explicit expression for the projection matrix is needed in order to calculate the survival probability.

IV.2.1 The T-Shaped Ar_3 Projection Matrix

An explicit expression for the projection matrix

$$< \psi^j \,|\, \hat{h}(x) \,|\, \psi^k > = \int_{0+}^{\infty} dx \int_{-\infty}^{\infty} dy \; \psi^j(x,y)\, \psi^k(x,y) \quad , \tag{112}$$

can be determined by expanding the T-shaped Ar_3 energy eigenfunctions $\{\psi^j(x,y)\}$ in terms of the symmetrized DVR basis as

$$\psi^j(x,y) = \sum_{i,(x_i \geq 0)} c_i^j \; < x,y \,|\, i' > \quad , \tag{113}$$

where the basis functions $< x,y \,|\, i' >$ are defined in equation (22). Substituting this expression for an eigenfunction $\psi^j(x,y)$ into equation (112) and simplifying using

$$\int_{-\infty}^{\infty} dy \; < y \,|\, y_i >< y \,|\, y_l > = \frac{\delta_{y_i,y_l}}{\Delta y} \quad , \tag{114}$$

which is computed in Appendix A, plus defining the integrals

$$\int_{0+}^{\infty} dx \; < x \,|\, x_i >< x \,|\, x_l > \; = \Upsilon(x_i, x_l) \quad , \tag{115}$$

$$\int_{0+}^{\infty} dx \; < x \,|\, x_i >< x \,|\, \hat{R}x_l > \; = \Upsilon(x_i, \hat{R}x_l) \quad , \tag{116}$$

and so on; the projection matrix is now given by

$$< \psi^j \,|\, \hat{h}(x) \,|\, \psi^k > = \sum_{i,(x_i \geq 0)} \sum_{l,(x_l \geq 0)} \frac{c_i^j \; c_l^k}{\Delta y} \; \{\text{integral terms}\} \quad . \tag{117}$$

The notation {integral terms} means combinations of

$$k_1 \Upsilon(x_i, x_l) + k_2 \Upsilon(x_i, \hat{R}x_l) + k_3 \Upsilon(\hat{R}x_i, x_l) + k_4 \Upsilon(\hat{R}x_i, \hat{R}x_l) \quad , \tag{118}$$

and the sum is over all combinations of the symmetric and anti-symmetric coefficients, $c_i^{j^s}$ and $c_i^{j^a}$, on $x_i > 0$ and $x_i = 0$ (nine terms in total). The constants k_i have values of ± 1, which are different for each of the sums. These integrals are evaluated numerically by a Gauss-Legendre numerical integrator routine. The convergence of the integrals is on the order of 10^{-4}.

IV.3 A Statistical Model of the T-Shaped Ar_3 Survival Probability

Equations (110) and (118) clearly show the computational magnitude associated with quantum mechanical molecular dynamics. For each time t, the survival probability $C(t)$ involves a sum over the set of T-shaped Ar_3 energy eigenstates, and each term in this sum involves a double sum over the DVR grid-points. In addition to these computations there is a significantly intensive numerical integration, plus the matrix diagonalization which generated the eigenvalues and eigenfunctions in the first place. It is no wonder that fully quantum mechanical investigations into chemical processes involve few atoms (generally less than four are considered). It would be highly advantageous to develop a new scheme for extracting dynamical observables from a quantum system. A quantum statistical model of the T-shaped Ar_3 survival probability is evolved from the characteristic statistical properties of the energy eigenvalues and eigenfunctions. These statistical properties can be predicted for quantum analogues to classically chaotic systems. The model survival probability is based on generating a set of "random T-shaped Ar_3 energy eigenvalues" and a "random projection matrix" which together determine a "random survival probability".

IV.3.1 Random T-Shaped Ar_3 Energy Eigenvalues

A set of random T-shaped Ar_3 energy eigenvalues can be generated by simply inverting the semi-classical density of states curves. These random eigenvalues must contain all the same statistical properties found in the quantum spectrum. Specifically, the scaled energies of the random symmetric and anti-symmetric spectra must have a Wigner successive level spacing distribution. This same distribution is predicted for the eigenvalues of a Gaussian orthogonal ensemble of random matrices.

Random matrix theories [Me-91, BG-84] were developed to alleviate the problems encountered with a detailed description of energy levels when their number be-

comes impossibly large. In ordinary statistical mechanics only the overall behaviour of a set of levels is determined as it is assumed that all of the states in the large ensemble are equally probable. In order to describe the fine detail of a level structure, a new type of statistical mechanics is needed where exact knowledge not of the state of the system, but of the nature of the system is renounced. Wigner first introduced the idea of choosing a Hamiltonian matrix at random from a large sample of systems in which all possible laws of interaction are probable. The ensemble of Hamiltonians is specified by a probability density $P(H)\,dH$ and certain symmetry requirements, such as being Hermitian, which must be satisfied.

A Gaussian orthogonal ensemble requires that the ensemble is invariant under every orthogonal transformation

$$H' = W^T H W \quad , \tag{119}$$

where W is any real orthogonal matrix; therefore, the probability that a matrix H will be in the volume element dH is also invariant

$$P(H')\,dH' = P(H)\,dH \quad . \tag{120}$$

The matrix elements of the random Hamiltonian are also independent random variables. This requirement has no special physical origin, it is used to simplify the ensuing mathematical problem. These restrictions determine the probability density as

$$P(H)\,dH = K_n \exp\left(-\frac{Tr\,[H^2]}{\tau^2}\right) \quad , \tag{121}$$

where K_n is a normalization constant, n is the dimensionality of the matrix and

$$Tr\,[H^2] = \sum_{i,j} (H_{ij})^2 \quad . \tag{122}$$

The GOE depends only on a scale factor τ^2 and the dimensionality n; the matrix elements have a Gaussian distribution with zero mean. From the invariance properties

of the Hamiltonian matrix, the probability density of the random eigenvalues $\{\lambda_j\}$ is given by

$$\rho(\lambda_1, \lambda_2, \ldots, \lambda_n) = K_n \exp\left(-\sum_i \frac{\lambda_i^2}{\tau^2}\right) \Pi_{i<j} |\lambda_i - \lambda_j| \, \Pi_n \, d\lambda_n \quad . \tag{123}$$

Notice that when $\lambda_i = \lambda_j$ the probability density vanishes; *i.e.*, there is level repulsion. By integrating this equation over all but one variable, the average eigenvalue density is determined to be

$$\rho(\lambda) = \int d\lambda_2 \ldots \int d\lambda_n \, \rho(\lambda_1, \lambda_2, \ldots, \lambda_n) = \begin{cases} \frac{2}{n\pi\tau^2} \left(n\tau^2 - \lambda^2\right)^{\frac{1}{2}} & |\lambda| \leq \sqrt{n\tau^2} \\ 0 & |\lambda| \geq \sqrt{n\tau^2} \end{cases} \quad ; \tag{124}$$

this is known as the Wigner semi-circle law [Wi-57] for the level density of a random matrix.

A set of $n = 1000$ random eigenvalues was computed according to the probability density in equation (121). This involved initial construction of a spectrum in the interval $(-\sqrt{n}, \sqrt{n})$ followed by a random walk of each eigenvalue with the new value being accepted if the ratio of the densities

$$\frac{\rho(\lambda_{new})}{\rho(\lambda_{old})} > \chi \quad , \tag{125}$$

where χ is a randomly generated number between zero and one. After many iterations the set of random eigenvalues $\{\lambda_j\}$ converged to the semi-circle distribution given by equation (124); this is shown in Figure (23). The successive level spacing distribution for the scaled energies has the expected Wigner form, as seen in Figure (24). The set of randomly generated cumulative densities $N(\lambda_j)$ are used to interpolate random T-shaped Ar_3 energy eigenvalues from the semiclassical cumulative density of states curves, $\overline{N_s(E)}$ and $\overline{N_a(E)}$.

The model survival probability is based on symmetric and anti-symmetric energy levels which come in pairs (correlated) at below threshold energies, and are statistically independent or uncorrelated at above threshold energies. The random T-shaped Ar_3 energy eigenvalues $\{\tilde{E}_j\}$ are therefore comprised of paired levels $\{\tilde{E}_{j,s}(\lambda); E <$

$E_{thres}\}$ and $\{\tilde{E}_{j_a}(\lambda); E < E_{thres}\}$ generated by a set of random eigenvalues $\{\lambda_j\}$, and independent levels $\{\tilde{E}_{j_s}(\lambda); E > E_{thres}\}$ and $\{\tilde{E}_{j_a}(\lambda'); E > E_{thres}\}$ where the anti-symmetric levels are generated by a different set of random eigenvalues $\{\lambda'_j\}$.

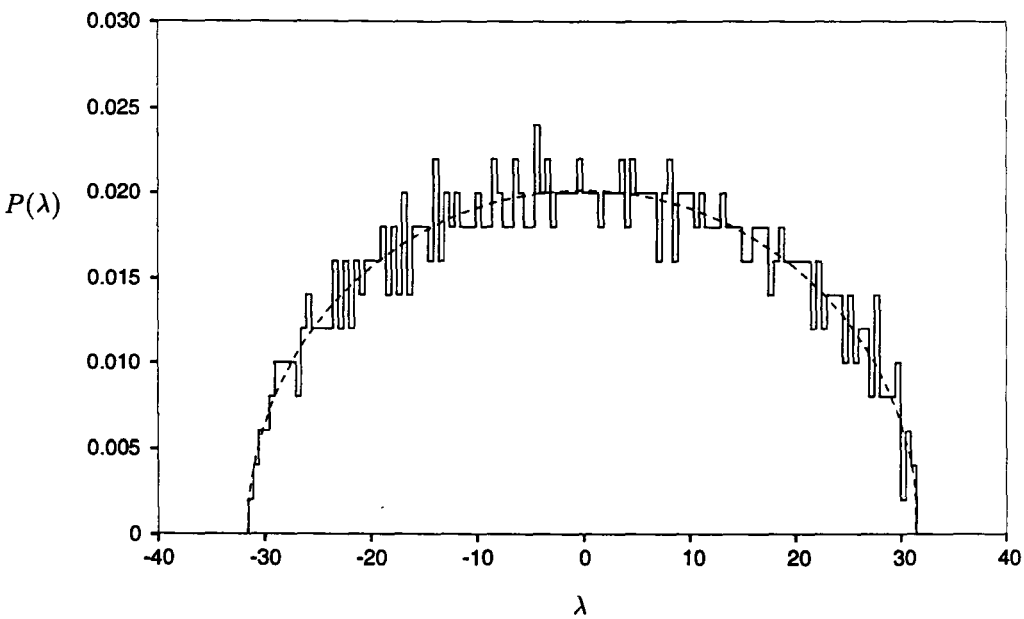

FIGURE 23. Probability distribution $P(\lambda)$ for the random eigenvalues $\{\lambda_j\}$.

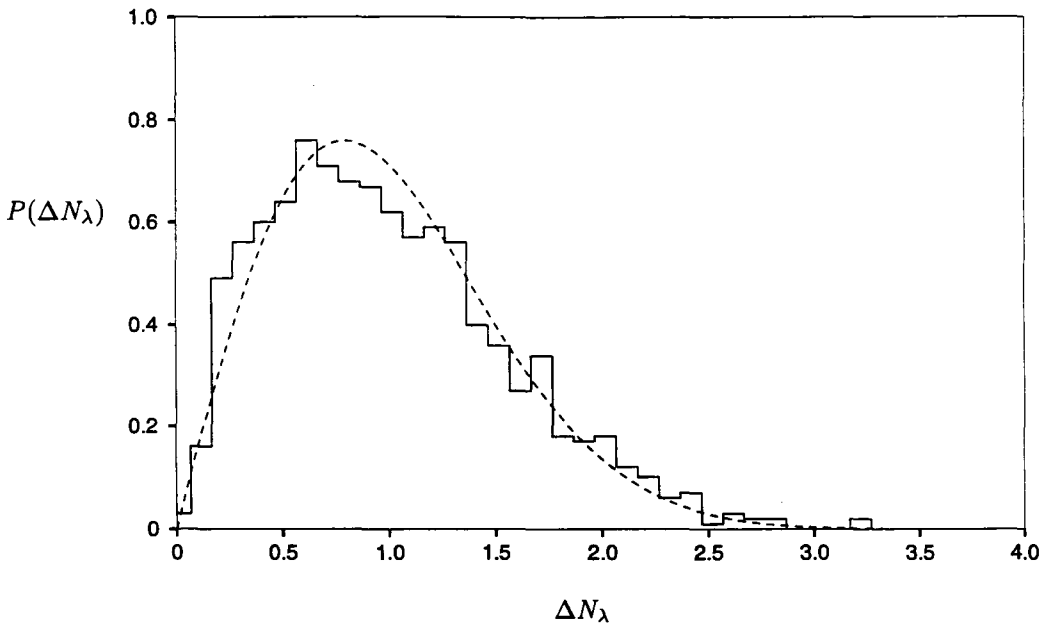

FIGURE 24. Successive level spacing distribution $P(\Delta N_\lambda)$ for the random eigenvalue spectrum $\{\lambda_j\}$. Superimposed is the Wigner (dashed) distribution.

IV.3.2 Random Projection Matrix

A statistical model for the projection matrix is based on the statistical properties of the symmetric and anti-symmetric T-shaped Ar_3 energy eigenfunctions which determine the properties of the T-shaped Ar_3 projection matrix. Since the projection matrix is symmetric, only the upper triangle need be determined. The matrix elements consist of connections between same symmetry and opposite symmetry states. In the case of connections between same symmetry states, the formula derived in Section IV.1.2 gives a simple expression for the matrix element as

$$\delta_{j,k} = (1+\kappa) < \psi^j(x,y) \,|\, \hat{h}(x) \,|\, \psi^k(x,y) > \quad , \tag{126}$$

where $\kappa = 1$ for same symmetry states. Thus, the same symmetry matrix elements are given by

$$< \psi^{j_s}(x,y) \,|\, \hat{h}(x) \,|\, \psi^{k_s}(x,y) > = < \psi^{j_a}(x,y) \,|\, \hat{h}(x) \,|\, \psi^{k_a}(x,y) > = \frac{\delta_{j,k}}{1+\kappa} = \begin{cases} 1/2 & j = k \\ 0 & j \neq k \end{cases} . \tag{127}$$

The block of matrix elements between opposite symmetry states is separated into below threshold and above threshold contributions. At below threshold energies, the symmetric and anti-symmetric T-shaped Ar_3 eigenvalues come in nearly degenerate pairs. The corresponding eigenfunctions are nearly identical except for an exponentially small correction from the small interval about $x = 0$. This correlation in the paired states is clearly demonstrated in Figure (25) which shows the spatial dependence between $\psi^{j_s}(x_i, y_i)$ and $\psi^{j_a}(x_i, y_i)$ at each grid-point (x_i, y_i) for $E_j < E_{thres}$. The model matrix element between the nearly degenerate opposite symmetry states can therefore be approximated by that of the same symmetry matrix elements,

$$< \psi^{j_s}(x,y) \,|\, \hat{h}(x) \,|\, \psi^{j_a}(x,y) > = \frac{1}{2} \qquad E_j < E_{thres} \quad . \tag{128}$$

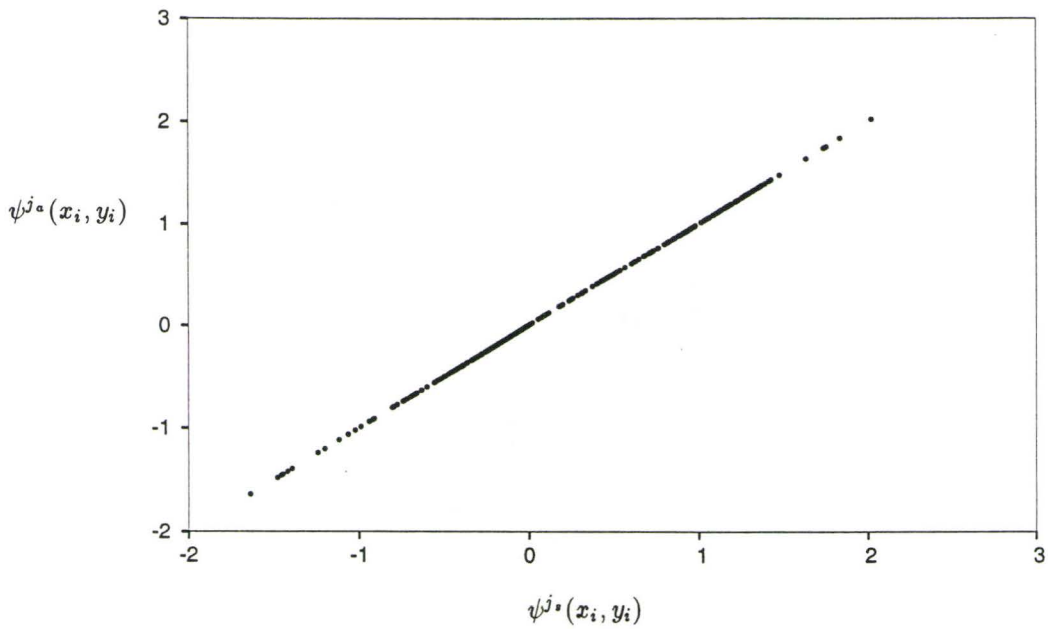

FIGURE 25. Spatial correlation between the paired symmetric and anti-symmetric T-shaped Ar_3 energy eigenfunctions at below threshold energies; $E_j = 136.44K$.

The off-diagonal matrix elements can be determined from an expression derived from the properties of the T-shaped Ar_3 projection matrix, which is given by

$$(E_{k_a} - E_{j_s}) < \psi^{j_s} \mid \hat{h}(x) \mid \psi^{k_a} > = \frac{\hbar^2}{2} \int_{\Re} dy \left(\psi^{j_s}(x,y) \frac{\partial}{\partial x} \psi^{k_a}(x,y) \right)_{x=0} . \qquad (129)$$

The support of an energy eigenfunction $\psi^j(x,y)$ is within the classically allowed region of configuration space where $E_j > V(x,y)$. Outside this region, the amplitude of the eigenfunction decays rapidly to zero. This is demonstrated in the wavefunction contour plots in Figure (26) for a below threshold energy eigenfunction.

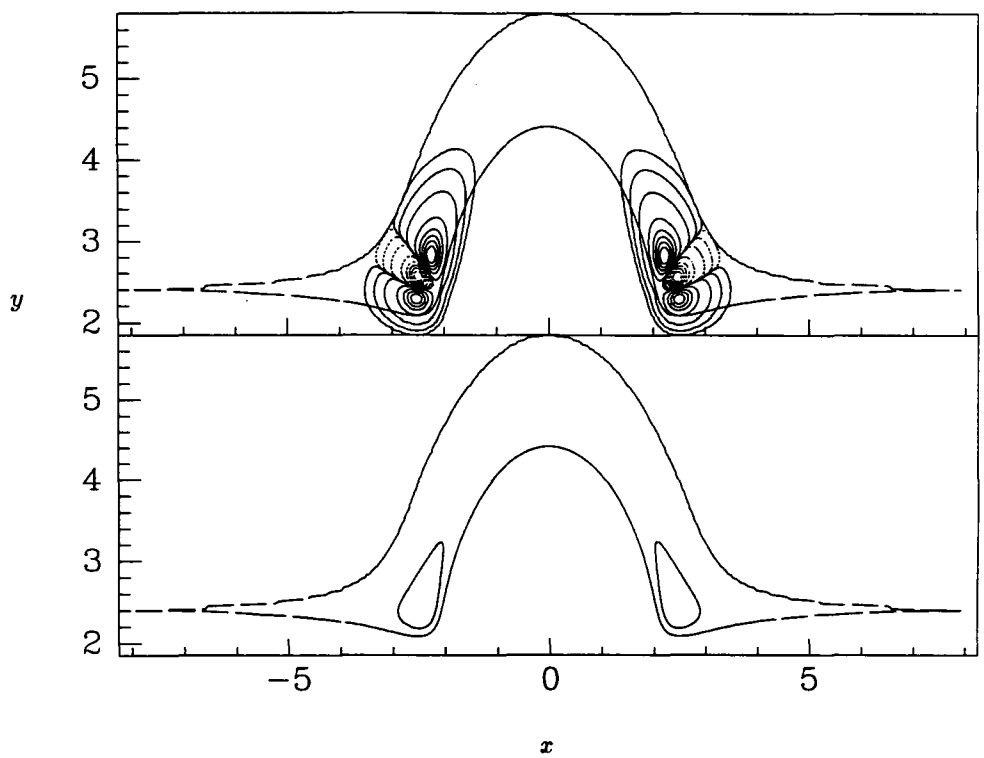

FIGURE 26. Wavefunction contour for a below threshold symmetric T-shaped Ar_3 energy eigenfunction ($E_{j_s} = 106.64K$) within the potential energy contour defined by $V(x_i, y_i) = E_{max} = 286K$. The wavefunction is almost entirely contained within the potential energy contour defined by $V(x_i, y_i) = E_{j_s}$ (the classically allowed region for ψ^{j_s}) in the lower figure.

The three lowest contours at the amplitude of 10^{-5} to 10^{-7} were added in Figure (26) to show that $\psi^{j_s}(x,y)_{x=0}$ is exponentially small at below threshold energies as $x = 0$ is outside the classically allowed region in configuration space. Thus, the right hand side of equation (129) is exponentially small, and since the energy splitting is not exponentially small the projection matrix element must be. The off-diagonal matrix elements between the opposite symmetry states at below threshold energies is therefore given by

$$< \psi^{j_s}(x,y) \,|\, \hat{h}(x) \,|\, \psi^{k_a}(x,y) > \simeq 0 \qquad E_j, E_k < E_{thres} \quad . \tag{130}$$

This same argument also leads to a zero matrix element between states when one state is above and the other is below threshold as one of the eigenfunctions $\psi^j(x,y)_{x=0}$ will be exponentially small. The only remaining case is projection matrix elements between two opposite symmetry states both at above threshold energies.

At above threshold energies, the definition of the projection matrix element in equation (112) is used to construct the model matrix elements. Since the above threshold T-shaped Ar_3 energy eigenfunctions could be described as Gaussian random variables, the projection matrix elements are also Gaussian random variables which are characterized by the variance,

$$\begin{aligned} \mathrm{var}\left(< \psi^{j_s}(x,y) \,|\, \hat{h}(x) \,|\, \psi^{k_a}(x,y) > \right) &= \overline{(h_{j_s,k_a})^2} - (\overline{h_{j_s,k_a}})^2 \\ &= \overline{(h_{j_s,k_a})^2} \end{aligned} \quad , \tag{131}$$

as $\overline{\psi^j(x,y)} = 0$ from Figures (18) and (19), *i.e.*, the projection matrix element itself has a zero mean. Substituting equation (112) into equation (131) gives

$$\mathrm{var}(h_{j_s,k_a}) = \int_{x>0} dx\, dy \int_{x>0} dx'\, dy' \, \overline{\psi^{j_s}(x,y)\, \psi^{k_a}(x,y)\, \psi^{j_s}(x',y')\, \psi^{k_a}(x',y')} \quad , \tag{132}$$

where the averaging is taken inside the integration. This expression is simplified because the above threshold eigenfunctions are assumed to be statistically independent,

thus

$$\overline{\psi^{j_s}\,\psi^{k_a}} = \overline{\psi^{j_s}}\;\overline{\psi^{k_a}} \quad , \tag{133}$$

and the variance is now given by

$$\mathrm{var}(h_{j_s,k_a}) = \int_{x>0} dx\,dy \int_{x>0} dx'\,dy'\; \overline{\psi^{j_s}(x,y)\,\psi^{j_s}(x',y')}\;\overline{\psi^{k_a}(x,y)\,\psi^{k_a}(x',y')} \quad . \tag{134}$$

These averaged quantities are none other than the spatial pair-correlation functions of Section III.2.2; therefore, the correlations of ψ^{j_s} and ψ^{k_a} can be replaced by Berry's formula in equation (70) to determine the variance of the projection matrix element as

$$\mathrm{var}(h_{j_s,k_a}) = \int_{x>0} dx\,dy \int_{x>0} dx'\,dy'\; \frac{J_0\left[\sqrt{2(E_{j_s}-V(r^\circ))}\,\frac{r'}{\hbar}\right]}{2A_{j_s}}\;\frac{J_0\left[\sqrt{2(E_{k_a}-V(r^\circ))}\,\frac{r'}{\hbar}\right]}{2A_{k_a}} \quad , \tag{135}$$

In terms of the DVR grid, the variance of the projection matrix element between above threshold opposite symmetry states is

$$\mathrm{var}(h_{j_s,k_a}) = \frac{(\Delta x\,\Delta y)^2}{4A_{j_s}A_{k_a}} \sum_{x_i\geq 0}\sum_{x_j\geq 0} J_0\left[\sqrt{2(E_{j_s}-V(r^\circ_{i,j}))}\,\frac{r'_{i,j}}{\hbar}\right] J_0\left[\sqrt{2(E_{k_a}-V(r^\circ_{i,j}))}\,\frac{r'_{i,j}}{\hbar}\right] \quad . \tag{136}$$

The sums over the DVR grid-points can be reduced to only those grid-points contained within the contour defined by $V(x_i,y_i) = \min(E_{j_s},E_{k_a})$ as outside this region one of the $\psi^{j_s}(x,y)$ or $\psi^{k_a}(x,y)$ is exponentially small and therefore makes a vanishing contribution to the integral in equation (134).

Because the projection matrix elements are Gaussian random variables, the central limit theorem can be applied to determine the asymptotic form of the integral of equation (112) as

$$h_{j_s,k_a} = \overline{h_{j_s,k_a}} + [\mathrm{var}(h_{j_s,k_a})]^{\frac{1}{2}}\,\nu_{j_s,k_a} \quad , \tag{137}$$

where ν_{j_s,k_a} is a Gaussian random variable with zero mean and unit variance. The random projection matrix element is therefore given by

$$h_{j_s,k_a} = [\mathrm{var}(h_{j_s,k_a})]^{\frac{1}{2}}\,\nu_{j_s,k_a} \quad , \tag{138}$$

as $\overline{h_{j_s,k_a}} = 0$. The upper triangle of the projection matrix is shown below where the matrix elements arise from equations (127), (128), (130) and (138);

$$h_{j,k} = \begin{array}{c} \\ \\ \\ \\ \\ \\ \\ \\ \\ \\ \\ \\ \\ \\ \end{array} \begin{array}{c} \begin{array}{cccccc} & & & & & E < E_{thres} \end{array} \\ \left(\begin{array}{cccccc|ccccc} \frac{1}{2} & 0 & \cdots & \cdots & \cdots & 0 & \frac{1}{2} & & 0 & 0 & \cdots & 0 \\ & \ddots & \ddots & & & \vdots & & \ddots & & \vdots & \ddots & \vdots \\ & & \frac{1}{2} & \ddots & & \vdots & 0 & & \frac{1}{2} & 0 & \cdots & 0 \\ & & & \frac{1}{2} & \ddots & \vdots & 0 & \cdots & 0 & & & \\ & h_{j_s,k_s} & & & \ddots & 0 & \vdots & \ddots & \vdots & & h_{j_s,k_a} & (138) \\ & & & & & \frac{1}{2} & 0 & \cdots & 0 & & & \\ - & - & - & - & - & - & - & - & - & - & - & - \\ & & & & & & \frac{1}{2} & 0 & \cdots & \cdots & \cdots & 0 \\ & & & & & & & \ddots & \ddots & & & \vdots \\ & & & & & & & & \frac{1}{2} & \ddots & & \vdots \\ & & & & & & & & & \frac{1}{2} & \ddots & \vdots \\ & & & & & & & h_{j_a,k_a} & & & \ddots & 0 \\ & & & & & & & & & & & \frac{1}{2} \end{array} \right) \\ \begin{array}{cccccc} & & & & & E > E_{thres} \end{array} \end{array} \quad . \tag{139}$$

The normalization properties of the same symmetry block are consistent with that of the T-shaped Ar_3 projection matrix, *i.e.*,

$$\sum_{j \text{ or } k} (h_{j,k})^2 = \frac{1}{4} \quad . \tag{140}$$

The below threshold elements of the opposite symmetry block h_{j_s,k_a} are also normalized as above. However, the above threshold elements given by equation (138) do not produce a normalized matrix.

The above threshold opposite symmetry matrix elements are row/column normalized by a random orthogonal matrix routine. An initial random matrix was constructed with elements given by

$$h_{j_s,k_a} = [\text{var}(h_{j_s,k_a})]^{\frac{1}{2}} \quad ; \tag{141}$$

note that this is equation (138) but without the Gaussian random variable ν_{j_s,k_a}. Each of these elements are randomly walked based on a Gaussian density and are constrained at each step to the normalization requirement. This routine produces a normalized above threshold opposite symmetry projection matrix with elements which are Gaussian distributed to the extent allowed by the normalization constraint. Although the matrix elements do not arise from a strict application of the central limit theorem from equation (137), the normalization property of the projection matrix is required such that a random survival probability calculated with a normalized random projection matrix can be compared to the quantum survival probability calculated with a normalized projection matrix. The T-shaped Ar_3 survival probability given in equation (110) was calculated for both the quantum mechanical eigenvalues and projection matrix and the statistical model to these quantities; the results are presented in the following section.

IV.4 Quantum and Random T-Shaped Ar_3 Survival Probability

In the energy representation, the survival probability $C(t)$ is expressed as

$$C(t) = \frac{1}{Q}\left\{\sum_j \exp(-\beta E_j)\,|<\psi^j\,|\,\hat{h}(x)\,|\,\psi^j>|^2 + \sum_{j<k} 2\exp\left(-\frac{\beta(E_j+E_k)}{2}\right)\cos\left[\frac{(E_j-E_k)\,t}{\hbar}\right]|<\psi^j\,|\,\hat{h}(x)\,|\,\psi^k>|^2\right\} \quad . \tag{142}$$

Survival probabilities were calculated for an ensemble of T-shaped Ar_3 states at a temperature T initially located on $x > 0$ configuration space. The survival probability is interpreted as the probability at a time t the enemble remains at $x > 0$, *i.e.*, no inversion.

The statistical model of the survival probability assumed perfect correlation between the paired symmetric and anti-symmetric states at below threshold energies. This reflected the fact that the T-shaped Ar_3 symmetric and anti-symmetric energy levels were nearly degenerate (hence the corresponding eigenfunctions were nearly

identical $\rightarrow$ highly correlated) at $E_j < E_{thres}$. The perfect correlation contained in the below threshold statistical model manifests degenerate (zero splittings) random T-shaped Ar_3 energy levels and a diagonal ($h_{j,k} = \delta_{j,k}/2$) random projection matrix.

Because of convergence error in the DVR method, the very small splittings in the below threshold paired T-shaped Ar_3 energy levels were not accurately determined. The size of the splitting can be estimated from equation (103) which relates the energy splitting $E_{k_a} - E_{j_s}$ to the projection matrix element h_{j_s,k_a} and the boundary surface overlap integral of $(\psi^{j_s}(x,y)\frac{\partial}{\partial x}\psi^{k_a}(x,y))_{x=0}$. The splittings predicted from this formula were found to be orders of magnitude smaller than actually obtained (especially for the lowest lying eigenvalue pairs). The T-shaped Ar_3 eigenvalues were therefore approximated as degenerate by setting $E_{j_a} = E_{j_s}$ at below threshold. However, this perfect correlation was not encompassed into the corresponding eigenfunctions and hence not reflected in the T-shaped Ar_3 projection matrix. The below threshold projection matrix elements are calculated as per equation (117) and is therefore not taken as strictly diagonal. But, since it is assumed that the T-shaped Ar_3 energy eigenfunction is more accurately converged than the corresponding eigenvalue, the below threshold T-shaped Ar_3 projection matrix between the opposite symmetry states is diagonal to within the exponentially small difference between the paired states. Any error arising with not associating perfectly correlated energy eigenfunctions with the degenerate energy eigenvalues would be negligible. The statistical model also further assumed no correlation between the above threshold symmetric and anti-symmetric states.

The quantum and "renormalized" random T-shaped Ar_3 survival probability at a temperature of $T = 20K$ is shown in Figure (27). The temperature T determines what fraction of the ensemble is composed of below threshold energy states, and the

corresponding equilibrium value for the survival probability. These below threshold states can be thought of as the classically trapped states at $x > 0$ which correspond to a classical equilibrium value. The fraction of below threshold states can be determined from

$$\frac{Q_b}{Q} = \frac{\sum_j{}' \exp(-\beta E_j)\, h_{j,j}}{\sum_j \exp(-\beta E_j)\, h_{j,j}} = \frac{\sum_j{}' \exp(-\beta E_j)}{\sum_j \exp(-\beta E_j)} \quad , \tag{143}$$

where $h_{j,j} = 1/2$ and $\sum'$ is over states which have an energy $E_j < E_{thres}$. The equilibrium value of the survival probability is given by

$$C_{eq} = 1 - \frac{1 - \frac{Q_b}{Q}}{2} \quad ; \tag{144}$$

it is about this value that $C(t)$ fluctuates at long times t. Since the below threshold spectrum for the T-shaped Ar_3 and random T-shaped Ar_3 energy eigenvalues are different, the fraction of below threshold states, f_b(Quantum) and f_b(Random) respectively, will also be different, and hence so will the corresponding equilibrium values. A comparison of the two methods requires a normalized survival probability $\tilde{C}(t)$ which is expressed as

$$C(t) = f_b + (1 - f_b)\,\tilde{C}(t) \qquad \begin{array}{ll} \text{random } C(t): & f_b = f_b(R) \\ \text{quantum } C(t): & f_b = f_b(Q) \end{array} \quad ; \tag{145}$$

with the normalized equilibrium value $\tilde{C}_{eq} = 1/2$ in both cases. Alternatively, the random survival probability is renormalized such that it fluctuates about the same equilibrium value as the quantum survival probabilty by constructing a new random survival probability $C'(t)$ from the normalized random survival probability $\tilde{C}(t)$ and the fraction of below threshold quantum states $f_b(Q)$

$$C'(t) = f_b(Q) + (1 - f_b(Q))\,\tilde{C}(t) \quad . \tag{146}$$

Substituting equation (145) for the random survival probability $C(t)$ then the renormalized random survival probability is given by

$$C'(t) = f_b(Q) + (1 - f_b(Q))\,\frac{C(t) - f_b(R)}{1 - f_b(R)} \quad . \tag{147}$$

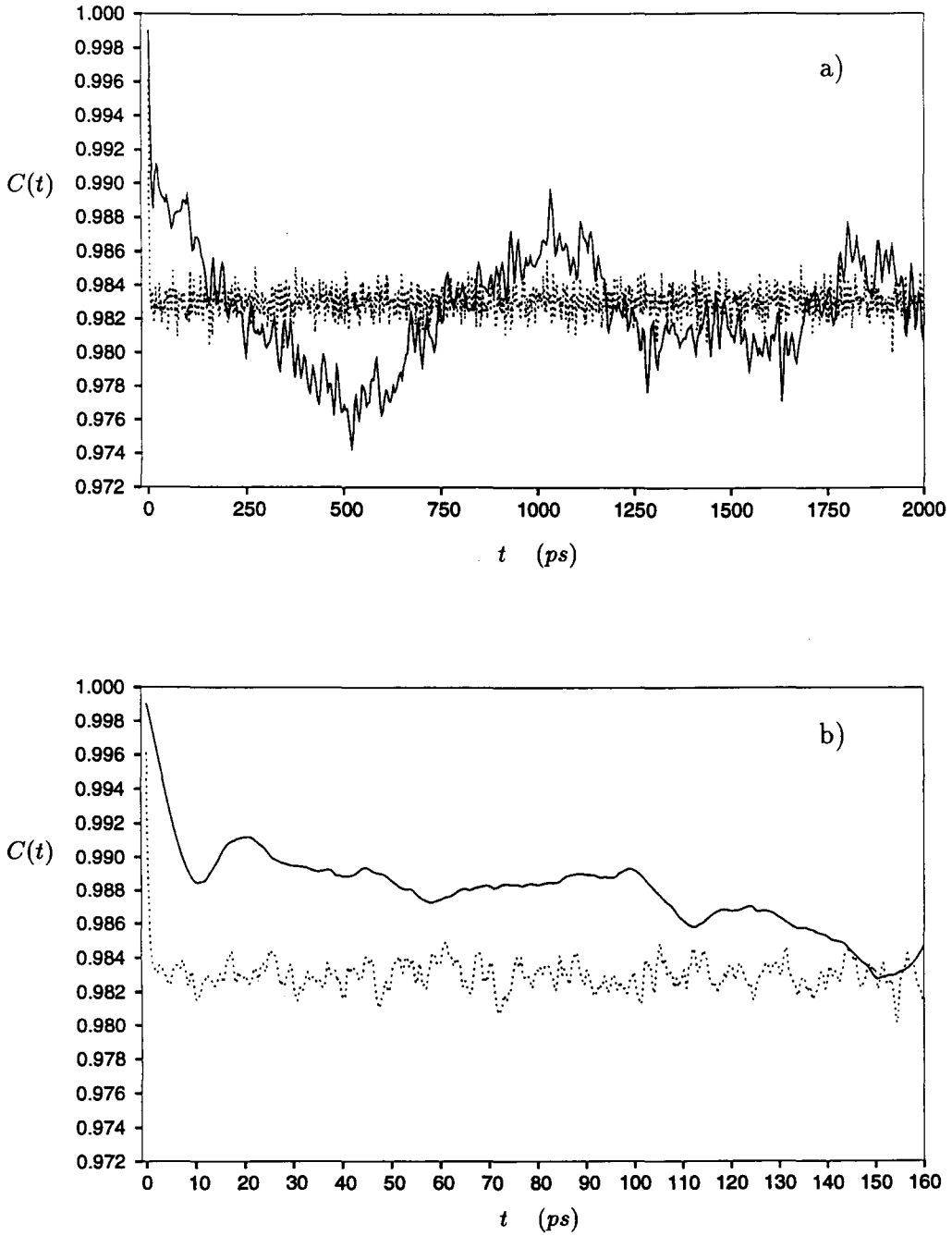

FIGURE 27. Quantum (solid) and random (dotted) survival probablity curves at temperature $T = 20K$ for a) long times t and b) short times t.

The discrepency between the two curves can be explained through a closer examination of the formula for $C(t)$ in equation (142). The dynamical (time) dependence of the survival probability originates in the cosine term, $\cos\left[\frac{(E_j-E_k)t}{\hbar}\right]$. This term produces the oscillations in $C(t)$ which are called "frequency beats" or "time scales" that are associated with the energy splittings $E_j - E_k$. The quantum survival probability in Figure (27a) appears to have two such time scales. The associated energy splittings with these time scales can be evaluated as the period of one oscillation is 2π for the cosine function. Therefore, the time scale of $800ps \rightarrow 1200ps$ is associated with the energy splittings in the range of $2.3K \rightarrow 3.4K$, and the time scale of $50ps$ and less corresponds to the energy range of splittings greater than $50K$. The random survival probability only shows the one short time scale for the larger energy splittings. This absence of the longer time scale plus the faster decay of the random survival probability as seen in Figure (27b) at small times are a consequence of the assumption of statistically independent above threshold symmetric and anti-symmetric states.

The statistical model was based on symmetric and anti-symmetric states which are perfectly correlated at below threshold energies and uncorrelated at above threshold energies. This terminus at threshold of the highly correlated paired states is not observed in the T-shaped Ar_3 spectrum. There is "residual" pairing and associated correlation between symmetric and anti-symmetric eigenfunctions just above threshold. This is clearly demonstrated in Figure (28) which shows the spatial correlation between a "paired" symmetric and anti-symmetric energy eigenfunction at above threshold.

The residual pairing of the states above threshold is reflected in the T-shaped Ar_3 projection matrix as elements between these states are near 1/2. Figure (29) shows the square of the projection matrix elements between a near threshold symmetric state

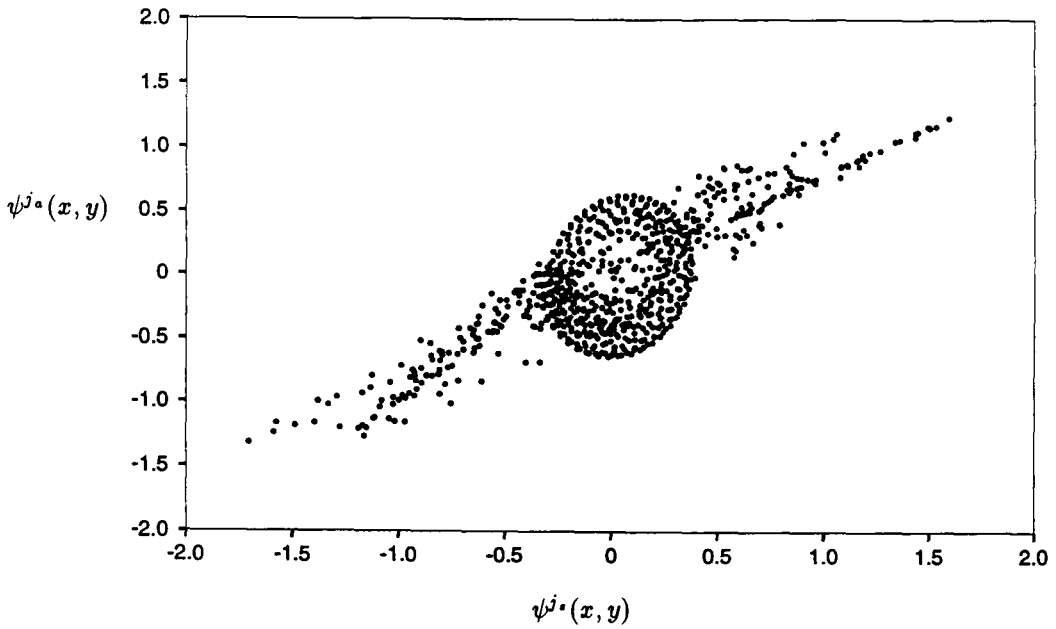

FIGURE 28. Spatial correlation between the residually paired symmetric and anti-symmetric T-shaped Ar_3 energy eigenfunctions at above threshold energies; $E_j = 163.01K$.

in the j_s^{th} row to each k_a^{th} anti-symmetric state. The random projection matrix does not encompass the correlations in the above threshold paired states as its elements at small energy splittings is much less than the correlated value at 1/2. The effect of no correlation in the random projection matrix elements at near threshold energies is the absence of the long time scale associated with the small energy splittings ($\Delta E < 10K$). Although the mean energy splitting is one, it is the small splittings occurring from near threshold states that are favoured by the Boltzmann factor in equation (142); consequently the "correlated" T-shaped Ar_3 projection matrix element between these states is a dominant contribution to the survival probability, and hence the observed long time scale. Meanwhile, the near threshold small splittings are not re-inforced in the random projection matrix because the corresponding elements are an order of

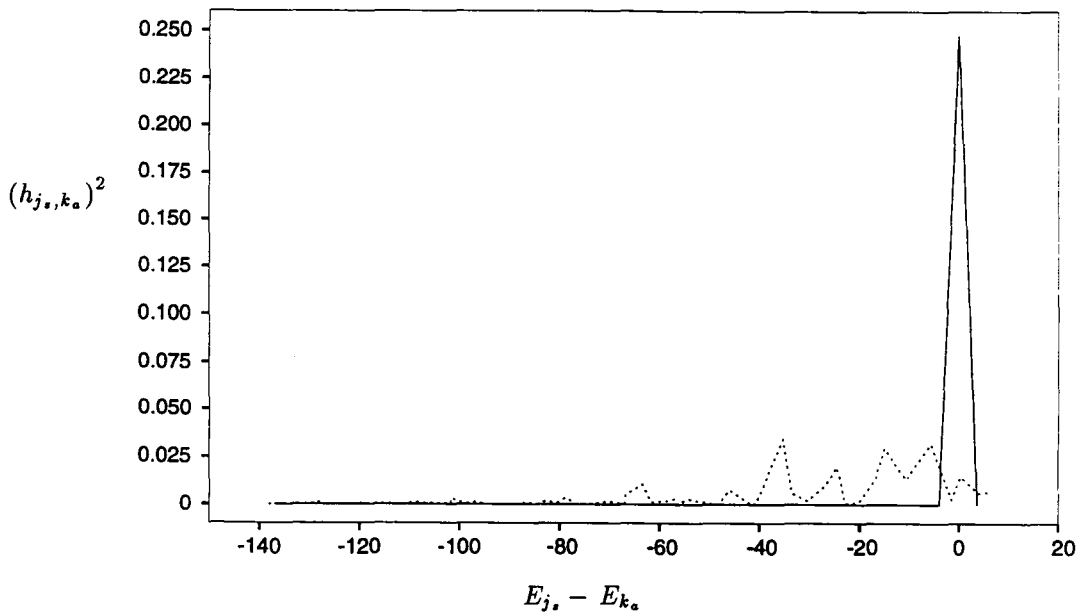

FIGURE 29. The quantum (solid) and random (dotted) projection matrix elements squared along the $E_{j_s} = 147K$ row to each k_a^{th} anti-symmetric state.

magnitude less, resulting in no long time scale in the random survival probability. Further note that there is no dynamical contribution to the quantum and random survival probability from the paired below threshold states as they were approximated as exactly degenerate. Therefore, this time scale from the below threshold small splittings is not observed in Figure (27) as it occurs for $t \to \infty$.

At small times t, only the larger energy splittings will appreciabely change (relative to the scale of the overall decay) the cosine term in $C(t)$ from its time zero value of one; therefore, it is only the larger energy splittings which contribute to the small time survival probability. The square of the projection matrix elements along the j_s^{th} row associated with larger energy splittings between the above threshold opposite symmetry states is shown in Figure (30). The random projection matrix

elements are larger than the quantum elements at the larger energy splittings. It is these contributions which result in the faster decay of the random survival probability compared to the quantum survival probability in Figure (27b) at small times. The rate of decay can be linked to the width of a Gaussian envelope over the peaks in Figure (30); a smaller width corresponds to a slower decay to the equilibrium value.

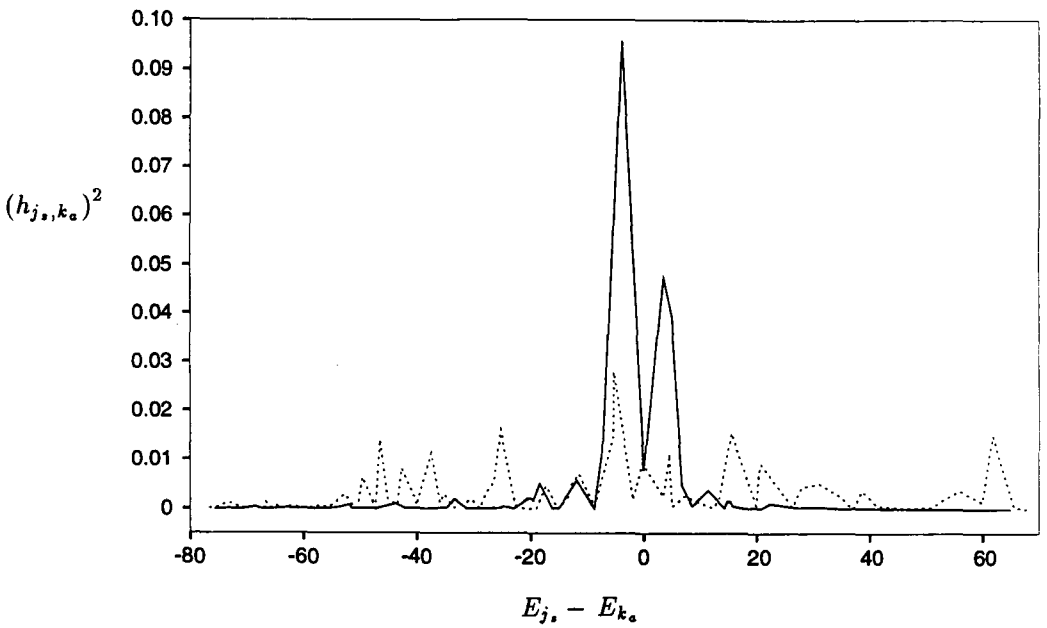

FIGURE 30. The quantum (solid) and random (dotted) projection matrix elements squared along the $E_{j_\bullet} = 209K$ row to each k_a^{th} anti-symmetric state.

Survival probabilities were also determined at a temperature of $T = 50K$; these curves were not qualitatively different from Figure (27) at the lower temperature. The statistical theory cleary needs to encorporate the residual pairing and associated correlations in the above threshold opposite symmetry eigenstates.

PART V

Summary

PART V

Summary

A statistical model of the T-shaped Ar_3 survival probability did not produce the long-time oscillatory behaviour of the survival probability determined by a full scale quantum mechanical description. The assumption of independent above threshold T-shaped Ar_3 eigenstates was the weak link in the statistical theory.

The intent of this research project was to develop a quick and easy method of calculating dynamical observables in a quantum system. A completely quantum mechanical treatment of molecular dynamics is never quick and easy, and can get downright hopeless for a many degree of freedom system. However, the use of a discrete variable representation for the T-shaped Ar_3 Hamiltonian allowed reasonably accurate calculations of the survival probability for the inversion process. The time and memory bottleneck in this procedure was in the evaluation of the projection matrix which involved a double sum over the DVR grid for each matrix element between two states.

A new route to quantum molecular dynamics was proposed on the basis of the observed statistical properties in the energy spectrum and wavefunctions of systems having a classically chaotic analogue. The classically chaotic dynamics of T-shaped Ar_3 was shown to exhibit these characteristic statistical properties. Specifically, the successive level spacing distribution of the T-shaped Ar_3 scaled symmetric and anti-symmetric energy spectra were shown to find good agreement with the Wigner distribution. This distribution is a property of the eigenvalues for a Gaussian orthogonal

ensemble of random matrices and has been observed for the energy spectra of classically chaotic systems. The T-shaped Ar_3 energy eigenfunctions were also seen to be Gaussian distributed with a spatial pair-correlation function approximated by a zeroth-order Bessel function. These results were predicted by Berry on the assumption that the chaotic eigenfunctions are Gaussian random variables in configuration space.

These statistical properties were used to construct a statistical model to the survival probability through the generation of random T-shaped Ar_3 energy eigenvalues and a random T-shaped Ar_3 projection matrix. The random T-shaped Ar_3 energy eigenvalues were constructed from a set of random eigenvalues for a Gaussian orthogonal ensemble of random matrices. Simple interpolation of the "scaled" random eigenvalues on the semi-classical density of states curves for the symmetric and anti-symmetric T-shaped Ar_3 spectra determined a set of random T-shaped Ar_3 energy eigenvalues. These random eigenvalues displayed all the same characteristic statistical properties of the quantum spectra. A random projection matrix was constructed based on the properties of the T-shaped Ar_3 energy eigenfunctions and the properties of the T-shaped Ar_3 projection matrix. The statistical model assumed perfectly correlated below threshold eigenstates and uncorrelated above threshold eigenstates. The former assumption which determined a diagonal same symmetry random projection matrix block of elements and a diagonal below threshold opposite symmetry block of elements accurately modeled the corresponding elements in the quantum system. However, the above threshold opposite symmetry random projection matrix elements were constructed on the assumption of statistically independent Gaussian random eigenstates at these energies. This simply is not observed in the T-shaped Ar_3 energy eigenfunctions as they are clearly correlated at above threshold energies

(Figure 28). Not accounting for these correlations in the statistical theory resulted in the random survival probabilty missing the long-time scale oscillation associated with the small energy splittings occuring from the residually paired near threshold states. This error also lead to the faster decay of the random survival probability at small times. Clearly, a useful statistical theory would need to encompass these correlations as a correction to the current model. Success is rarely a totality in any approximation to quantum mechanics – a statistical quantum dynamics based on the properties of the energy eigenvalues and eigenfunctions of a classically chaotic system may yet be realizable.

Future work should be taken to a system having a larger number of states so as to avoid any problems resulting from dealing with a limited set and to possibly identify energy ranges over which correlation effects are dominant. Of course, moving to a larger system would incur a longer computation time, but the rate of increase would still be orders of magnitude less than the corresponding quantum mechanical calculation. In fact, this statistical theory is hoped to find its greatest use on systems having a larger number of degrees of freedom, and perhaps on semi-classical limit calculations.

REFERENCES

REFERENCES

[1] a) Energy is measured in units of Kelvin (K) via scaling by Boltzmann's constant, $k_B = 1.38 \times 10^{-23} J/K$.
b) The atomic unit of time consistent with energy units of K is $\hbar/K$; $1\,\hbar/K = 7.6383\,ps$. The times reported here are in ps.
c) Distance is measured in the mass-scaled unit of ms-Bohr:
in the x-direction; 1 ms-Bohr $= 1.3489 \times 10^{-8}$ cm,
in the y-direction; 1 ms-Bohr $= 1.5578 \times 10^{-8}$ cm.

[AS-86] R.A. AZIZ, M.J. SLAMAN, Mol.Phys. **58** (1986) 679.

[AS-91] R. AURICH, F. STEINER, Physca.D. **48** (1991) 445.

[Be-77] M.V. BERRY, J.Phys.A **10** (1977) 2083.

[Be-85] M.V. BERRY, Proc.R.Soc.Lon. **A400** (1985) 229.

[BG-84] O. BOHIGAS, M.J. GIANNONI, *Mathematical and Computational Methods in Nuclear Physics*, Springer-Verlag, New York, 1984.

[BGS-84a] O. BOHIGAS, M.J. GIANNONI, C. SCHMIT, Phys.Rev.Let. **52** (1984) 1.

[BGS-84b] O. BOHIGAS, M.J. GIANNONI, C. SCHMIT, J.Phys.Let. **45** (1984) L1015.

[BLB-88] T.L. BECK, D.M. LEITNER, R.S. BERRY, J.Chem.Phys. **89** (1988) 1681.

[BT-77] M.V. BERRY, M. TABOR, Proc.R.Soc.Lon.Ser. **A356** (1977) 375.

[CM-92] D.T. COLBERT, W.H. MILLER, J.Chem.Phys. **96** (1992) 1982.

[DG-86] D. DELANDE, J.C. GAY, Phys.Rev.Let. **57** (1986) 2006.

[LHL-85] J.C. LIGHT, I.P. HAMILTON, J.V. LILL, J.Chem.Phys. **82** (1985) 1400.

[LSW-92] B.L. LAN, A. SHUSHIN, D.M. WARDLAW, Phys.Rev.A **46** (1992) 1775.

[MST-83] W.H. MILLER, S.D. SCHWARTZ, J.W. TROMP, J.Chem.Phys. **79** (1983) 4889.

[Me-91] M.L. MEHTA, *Random Matrices*, Acedemic Press, 1991.

[Ob-90] F. OBERHETTINGER, *Tables of Fourier Transforms and Fourier Transforms of Distributions*, Springer-Verlag, Berlin, 1990.

[SG-84] M. SHAPIRO, G. GOELMAN, Phys.Rev.Let. **53** (1984) 1714.

[Wi-56] E.P. WIGNER, *Conference on neutron physics by time-of-flight*, Tennessee, 1956

[Wi-57] E.P. WIGNER, Proc.Fourth.Can.Math.Con. (1957) 174.

APPENDIX A

T-Shaped Ar_3 Energy Eigenfunction Normalization

APPENDIX A

T-Shaped Ar_3 Energy Eigenfunction Normalization

The energy eigenfunctions of T-shaped Ar_3 can be expressed as an expansion in the symmetrized DVR basis functions at the grid-point $i = (x_i, y_i)$, namely

$$\psi^j(x,y) = \sum_{i,(x_i \geq 0)} c_i^j < x,y \,|\, i' > \quad , \tag{A1}$$

where

$$< x,y \,|\, i' > = \begin{cases} \frac{1}{\sqrt{2}} \left\{ < x,y \,|\, i > \pm < x,y \,|\, \hat{R}i > \right\} & x_i \neq 0 \\ < x,y \,|\, i > & x_i = 0 \end{cases} \quad , \tag{A2}$$

and

$$< x,y \,|\, i > = < x \,|\, x_i > < y \,|\, y_i > = \frac{\sin\left(\frac{\pi[x-x_i]}{\Delta x}\right)}{\pi[x-x_i]} \frac{\sin\left(\frac{\pi[y-y_i]}{\Delta y}\right)}{\pi[y-y_i]} \quad . \tag{A3}$$

The normalization condition is given by

$$\int_{-\infty}^{\infty} dx\, dy\, \psi^{j\,*}(x,y)\, \psi^k(x,y) = < \psi^j(x,y) \,|\, \psi^k(x,y) > = \delta_{j,k} \quad . \tag{A4}$$

Substituting the expansion from equation (A1) determines

$$\begin{aligned} < \psi^j(x,y) \,|\, \psi^k(x,y) > = \int_{-\infty}^{\infty} dx\, dy \Bigg[& \sum_{i,(x_i>0)} c_i^j \left\{ < x,y \,|\, i > \pm < x,y \,|\, \hat{R}i > \right\} \\ & + \sum_{i,(x_i=0)} c_i^j < x,y \,|\, i > \Bigg] \times \Bigg[\sum_{l,(x_l>0)} c_l^k \left\{ < x,y \,|\, l > \pm < x,y \,|\, \hat{R}l > \right\} \\ & + \sum_{l,(x_l=0)} c_l^k < x,y \,|\, l > \Bigg] \; ; \end{aligned} \tag{A5}$$

inserting the DVR basis functions from equation (A3) and factoring determines integrals of the form

$$\int_{-\infty}^{\infty} dx \, < x \,|\, x_i > < x \,|\, x_l > \int_{-\infty}^{\infty} dy \, < y \,|\, y_i > < y \,|\, y_l > \quad . \tag{A6}$$

Only the integration over dx will be explicity shown – the details for the dy integration are the same. A change of variables via

$$u = \frac{\pi(x - x_i)}{\Delta x} \qquad v = \frac{\pi(x_i - x_l)}{\Delta x} \quad , \tag{A7}$$

gives the equation

$$\int_{-\infty}^{\infty} dx < x \,|\, x_i >< x \,|\, x_l > = \int_{-\infty}^{\infty} dx \, \frac{\sin\left(\frac{\pi[x-x_i]}{\Delta x}\right)}{\pi[x - x_i]} \, \frac{\sin\left(\frac{\pi[x-x_l]}{\Delta x}\right)}{\pi[x - x_l]} = \int_{-\infty}^{\infty} du \, \frac{\sin(u)\sin(u+v)}{\pi \Delta x \, u\,(u+v)} \quad . \tag{A8}$$

From the relation

$$\sin(A + B) = \sin(A)\cos(B) + \sin(B)\cos(A) \quad , \tag{A9}$$

and since

$$\sin(v) = \sin\left(\frac{\pi(x_i - x_l)}{\Delta x}\right) = 0 \quad , \tag{A10}$$

as $\frac{(x_i - x_l)}{\Delta x} \in \aleph$, thus

$$\int_{-\infty}^{\infty} du \, \frac{1}{\pi \Delta x} \, \frac{\sin(u)}{u} \, \frac{\sin(u+v)}{u+v} = \int_{-\infty}^{\infty} du \, \frac{1}{\pi \Delta x} \, \frac{\sin(u)}{u} \, \frac{\sin(u)\cos(v)}{u+v} \quad . \tag{A11}$$

The cosine can be replaced by

$$\cos(v) = \cos\left(\frac{\pi(x_i - x_l)}{\Delta x}\right) = (-1)^{\frac{x_i - x_l}{\Delta x}} \quad ; \tag{A12}$$

this leaves the integral

$$\int_{-\infty}^{\infty} dx \; < x \,|\, x_i > < x \,|\, x_l > = \frac{1}{\pi \Delta x} \, (-1)^{\frac{x_i - x_l}{\Delta x}} \int_{-\infty}^{\infty} du \, \frac{\sin^2(u)}{u^2 + uv} \quad . \tag{A13}$$

While no closed form analytical expression was found, numerical integration revealed

$$\int_{-\infty}^{\infty} du \, \frac{\sin^2(u)}{u^2 + u(n\pi)} \simeq 0 \qquad \forall \quad n = 1, 2, \ldots \quad ; \tag{A14}$$

but for $n = 0$, *i.e.*, $x_i = x_l$, an analytical expression is given as

$$\int_{-\infty}^{\infty} du \, \frac{\sin^2(u)}{u^2} = \pi \quad . \tag{A15}$$

Therefore, the integration over dx is

$$\int_{-\infty}^{\infty} dx \; < x \,|\, x_i > < x \,|\, x_l > = \frac{1}{\pi \Delta x} (-1)^{\frac{x_i - x_l}{\Delta x}} \pi \, \delta_{x_i, x_l} = \frac{1}{\Delta x} \quad . \tag{A16}$$

The normalization condition is reduced to the expression

$$\begin{aligned} < \psi^j(x,y) \,|\, \psi^k(x,y) > \; = & \sum_{i,(x_i>0)} \sum_{l,(x_l>0)} \frac{c_i^j}{\sqrt{2}} \frac{c_l^k}{\sqrt{2}} \left\{ \frac{\delta_{x_i,x_l}}{\Delta x} \frac{\delta_{y_i,y_l}}{\Delta y} + \frac{\delta_{\hat{R}x_i,\hat{R}x_l}}{\Delta x} \frac{\delta_{\hat{R}y_i,\hat{R}y_l}}{\Delta y} \right\} \\ & + \sum_{i,(x_i=0)} \sum_{l,(x_l=0)} c_i^j \, c_l^k \, \frac{\delta_{x_i,x_l}}{\Delta x} \frac{\delta_{y_i,y_l}}{\Delta y} \quad . \end{aligned} \tag{A17}$$

Evaluation of the delta functions determines the normalization condition for an eigenfunction as

$$< \psi^j(x,y) \,|\, \psi^k(x,y) > = \sum_{i,(x_i>0)} \frac{c_i^j \, c_i^k}{\Delta x \, \Delta y} + \sum_{i,(x_i=0)} \frac{c_i^j \, c_i^k}{\Delta x \, \Delta y} = \sum_{i,(x_i \geq 0)} \frac{c_i^j \, c_i^k}{\Delta x \, \Delta y} = \delta_{j,k} \; . \tag{A18}$$

APPENDIX B

Properties of the T-Shaped Ar_3 Projection Matrix

APPENDIX B

Properties of the T-Shaped Ar_3 Projection Matrix

An expression for the projection matrix element h_{j_s,k_a} can be determined from the energy splitting, $E_{k_a} - E_{j_s}$. Consider the time independent Schrödinger equation

$$\hat{H}\psi^j = E_j\psi^j \quad ; \tag{B1}$$

the energy splitting between the symmetric state ψ^{j_s} and the anti-symmetric state ψ^{k_a} can be derived as follows: the equations

$$\hat{H}\psi^{j_s} = E_{j_s}\psi^{j_s} \quad , \tag{B2}$$

$$\hat{H}\psi^{k_a} = E_{k_a}\psi^{k_a} \quad ; \tag{B3}$$

are multiplied on the left by the opposite symmetry wavefunction and then subtracted to give

$$\begin{aligned} \psi^{j_s}\hat{H}\psi^{k_a} - \psi^{k_a}\hat{H}\psi^{j_s} &= \psi^{j_s}E_{k_a}\psi^{k_a} - \psi^{k_a}E_{j_s}\psi^{j_s} \\ &= (E_{k_a} - E_{j_s})\,\psi^{j_s}\psi^{k_a} \quad . \end{aligned} \tag{B4}$$

Integrating over the positive x-coordinate region of configuration space determines the expression

$$\begin{aligned} \int_{0+}^{\infty} dx \int_{-\infty}^{\infty} dy \left\{\psi^{j_s}\hat{H}\psi^{k_a} - \psi^{k_a}\hat{H}\psi^{j_s}\right\} &= (E_{k_a} - E_{j_s}) \int_{0+}^{\infty} dx \int_{-\infty}^{\infty} dy\, \psi^{j_s}\psi^{k_a} \\ &= (E_{k_a} - E_{j_s}) < \psi^{j_s} \,|\, \hat{h}(x) \,|\, \psi^{k_a} > \quad . \end{aligned} \tag{B5}$$

The projection matrix element can be evaluated explicity by substituting the form of the Hamiltonian given in equation (1), this determines the expression

$$\begin{aligned} (E_{k_a} - E_{j_s}) < \psi^{j_s} \,|\, \hat{h}(x) \,|\, \psi^{k_a} > = \int_{0+}^{\infty} dx \int_{-\infty}^{\infty} dy \Bigg\{ & \psi^{j_s} \left[\frac{\hat{p}_x^2}{2} + \frac{\hat{p}_y^2}{2} + \hat{V}(x,y) \right] \psi^{k_a} \\ & - \psi^{k_a} \left[\frac{\hat{p}_x^2}{2} + \frac{\hat{p}_y^2}{2} + \hat{V}(x,y) \right] \psi^{j_s} \Bigg\} \quad . \end{aligned} \tag{B6}$$

The potential energy terms cancel, leaving matrix elements of the kinetic energy operators

$$\hat{p}_x^2 = -\frac{\hbar^2}{2}\frac{\partial^2}{\partial x^2} \qquad \hat{p}_y^2 = -\frac{\hbar^2}{2}\frac{\partial^2}{\partial y^2} \quad , \tag{B7}$$

which can be written as

$$(E_{k_a} - E_{j_s}) < \psi^{j_s} | \hat{h}(x) | \psi^{k_a} > = -\frac{\hbar^2}{2}\int_{0+}^{\infty} dx \int_{-\infty}^{\infty} dy \left\{ \psi^{j_s} \nabla^2 \psi^{k_a} - \psi^{k_a} \nabla^2 \psi^{j_s} \right\} \quad , \tag{B8}$$

where ∇^2 is the Laplacian. From the simple relation

$$\psi^{j_s} \nabla^2 \psi^{k_a} = \nabla \cdot \left(\psi^{j_s} \nabla \psi^{k_a} \right) - \nabla \psi^{j_s} \cdot \nabla \psi^{k_a} \quad , \tag{B9}$$

then

$$\begin{aligned} (E_{k_a} - E_{j_s}) < \psi^{j_s} | \hat{h}(x) | \psi^{k_a} > = -\frac{\hbar^2}{2}\int_{0+}^{\infty} dx \int_{-\infty}^{\infty} dy \Big\{ & \nabla \cdot \left(\psi^{j_s} \nabla \psi^{k_a} \right) \\ & - \nabla \cdot \left(\psi^{k_a} \nabla \psi^{j_s} \right) \Big\} \quad , \end{aligned} \tag{B10}$$

where it is recognized that

$$\nabla \cdot \left(\psi^{j_s} \nabla \psi^{k_a} \right) = \mathrm{div} \left(\psi^{j_s} \nabla \psi^{k_a} \right) \quad , \tag{B11}$$

thus,

$$\begin{aligned} (E_{k_a} - E_{j_s}) < \psi^{j_s} | \hat{h}(x) | \psi^{k_a} > = -\frac{\hbar^2}{2}\int_{0+}^{\infty} dx \int_{-\infty}^{\infty} dy \Big\{ & \mathrm{div} \left(\psi^{j_s} \nabla \psi^{k_a} \right) \\ & - \mathrm{div} \left(\psi^{k_a} \nabla \psi^{j_s} \right) \Big\} \quad . \end{aligned} \tag{B12}$$

The integration over the positive x-coordinate region of configuration space of a divergence of a vector $\vec{F}$ can be thought of as a flow in or out of this region. This flow occurs along a boundary surface, which in this case is defined by the surface at $x = 0$. The divergence theorem equates the flow out of a region A to the flow across a boundary surface, S as

$$\int\int_A dx\, dy\, \mathrm{div}(\vec{F}) = \int_S d\sigma\, \vec{n}_\sigma \cdot \vec{F} \quad , \tag{B13}$$

where S is a positively oriented surface with outer unit normal n_σ. Equation (B12) therefore becomes,

$$(E_{k_a} - E_{j_s}) < \psi^{j_s} \,|\, \hat{h}(x) \,|\, \psi^{k_a} > = -\frac{\hbar^2}{2} \left\{ \int_S d\sigma \, \vec{n}_\sigma \cdot (\psi^{j_s} \nabla \psi^{k_a}) - \int_S d\sigma \, \vec{n}_\sigma \cdot (\psi^{k_a} \nabla \psi^{j_s}) \right\} \quad . \tag{B14}$$

The equation of the boundary surface can be written as

$$g(y) = x = 0 \quad \rightarrow \quad G(x,y) = x - g(y) = x \quad , \tag{B15}$$

and the normal unit vector $\tilde{n}$ to the surface is

$$\tilde{n} = \frac{\nabla G(x,y)}{|| \nabla G(x,y) ||} = \frac{\frac{\partial}{\partial x} G(x,y)\, \underline{\hat{x}} + \frac{\partial}{\partial y} G(x,y)\, \underline{\hat{y}}}{\left[\left(\frac{\partial}{\partial x} G(x,y) \right)^2 + \left(\frac{\partial}{\partial y} G(x,y) \right)^2 \right]^{\frac{1}{2}}} = \underline{\hat{x}} \quad , \tag{B16}$$

where $\underline{\hat{x}}$ and $\underline{\hat{y}}$ are the unit vectors directed along the positive x and y directions, respectively. Thus, the unit normal vector $\tilde{n}$ to the surface S points into the positive x-coordinate region of the region A in configuration space. The outer unit normal $\vec{n}_\sigma$ points away from A, therefore

$$\vec{n}_\sigma = -\tilde{n} = -\underline{\hat{x}} \quad , \tag{B17}$$

and equation (B14) becomes

$$(E_{k_a} - E_{j_s}) < \psi^{j_s} \,|\, \hat{h}(x) \,|\, \psi^{k_a} > = \frac{\hbar^2}{2} \left\{ \int_S d\sigma \, \underline{\hat{x}} \cdot (\psi^{j_s} \nabla \psi^{k_a}) - \int_S d\sigma \, \underline{\hat{x}} \cdot (\psi^{k_a} \nabla \psi^{j_s}) \right\} \quad . \tag{B18}$$

Upon evaluating the gradiant,

$$\nabla \psi = \frac{\partial}{\partial x} \psi \, \underline{\hat{x}} + \frac{\partial}{\partial y} \psi \, \underline{\hat{y}} \quad , \tag{B19}$$

then

$$(E_{k_a} - E_{j_s}) < \psi^{j_s} \,|\, \hat{h}(x) \,|\, \psi^{k_a} > = \frac{\hbar^2}{2} \left\{ \int_S d\sigma \, \psi^{j_s} \frac{\partial}{\partial x} \psi^{k_a} - \int_S d\sigma \, \psi^{k_a} \frac{\partial}{\partial x} \psi^{j_s} \right\} \quad , \tag{B20}$$

as $\hat{\underline{x}} \cdot \hat{\underline{y}} = 0$. For the boundary surface defined by $g(y) = x$ where $g(y)$ is a continuous function and has continuous first order partial derivative $g_y(y) = \frac{\partial}{\partial y} g(y)$, then for a continuous function $\Phi(x, y)$ on the region S there exists the relation

$$\int_S d\sigma \, \Phi(x,y) = \int_{\Re} dy \, \Phi(g(y), y) \sqrt{(g_y(y))^2 + 1} \quad , \tag{B21}$$

thus,

$$\begin{aligned} \frac{\hbar^2}{2} \left\{ \int_S d\sigma \, \psi^{j_*} \frac{\partial}{\partial x} \psi^{k_a} - \int_S d\sigma \, \psi^{k_a} \frac{\partial}{\partial x} \psi^{j_*} \right\} = \int_{\Re} dy \left\{ \left(\psi^{j_*} \frac{\partial}{\partial x} \psi^{k_a} \right)_{x=g(y)} \sqrt{(g_y(y))^2 + 1} \right. \\ \left. + \left(\psi^{k_a} \frac{\partial}{\partial x} \psi^{j_*} \right)_{x=g(y)} \sqrt{(g_y(y))^2 + 1} \right\} \quad . \end{aligned} \tag{B22}$$

The boundary surface is given by $g(y) = x = 0$, therefore $\frac{\partial}{\partial y} g(y) = 0$ and equation (B22) becomes

$$(E_{k_a} - E_{j_*}) < \psi^{j_*} \,|\, \hat{h}(x) \,|\, \psi^{k_a} > = \frac{\hbar^2}{2} \int_{\Re} dy \left\{ \left(\psi^{j_*} \frac{\partial}{\partial x} \psi^{k_a} \right)_{x=0} + \left(\psi^{k_a} \frac{\partial}{\partial x} \psi^{j_*} \right)_{x=0} \right\} \quad . \tag{B23}$$

Because of the properties of the T-shaped Ar_3 energy eigenfunctions in equations (82) and (83), then $\psi^{k_a}(x,y)_{x=0} = 0$ and $(\frac{\partial}{\partial x} \psi^{j_*}(x,y))_{x=0} = 0$. Consequently, the second term in equation (B23) vanishes leaving the expression

$$(E_{k_a} - E_{j_*}) < \psi^{j_*} \,|\, \hat{h}(x) \,|\, \psi^{k_a} > = \frac{\hbar^2}{2} \int_{\Re} dy \left(\psi^{j_*} \frac{\partial}{\partial x} \psi^{k_a} \right)_{x=0} \quad , \tag{B24}$$

which relates the projection matrix element h_{j_*,k_a} to the associated energy splitting and boundary surface overlap integral.